

Dispersive dark excitons in van der Waals ferromagnet CrI₃

W. He,^{1,*} J. Sears,¹ F. Barantani,² T. Kim,³ J. W. Villanova,⁴ T. Berlijn,⁴ M. Lajer,¹ M. A. McGuire,⁵ J. Pelliciani,³ V. Bisogni,³ S. Johnston,^{6,7} E. Baldini,² M. Mitrano,⁸ and M. P. M. Dean^{1,†}

¹*Department of Condensed Matter Physics and Materials Science,
Brookhaven National Laboratory, Upton, New York 11973, USA*

²*Department of Physics, The University of Texas at Austin, Austin, Texas, USA, 78712*

³*National Synchrotron Light Source II, Brookhaven National Laboratory, Upton, New York 11973, USA*

⁴*Center for Nanophase Materials Sciences, Oak Ridge National Laboratory, Oak Ridge, Tennessee 37831, USA*

⁵*Materials Science and Technology Division, Oak Ridge National Laboratory,
1 Bethel Valley Road, Oak Ridge, Tennessee 37831, USA*

⁶*Department of Physics and Astronomy, The University of Tennessee,
Knoxville, Tennessee 37966, USA*

⁷*Institute for Advanced Materials and Manufacturing, The University of Tennessee, Knoxville, Tennessee 37996, USA*

⁸*Department of Physics, Harvard University, Cambridge, Massachusetts 02138, USA*

(Dated: January 17, 2025)

Spin-flip dark excitons are optical-dipole-forbidden quasiparticles with remarkable potential in optoelectronics, especially when they are realized within cleavable van der Waals materials. Despite this potential, dark excitons have not yet been definitively identified in ferromagnetic van der Waals materials. Here, we report two dark excitons in a model ferromagnetic material CrI₃ using high-resolution resonant inelastic x-ray scattering (RIXS) and show that they feature narrower linewidths compared to the bright excitons previously reported in this material. These excitons are shown to have spin-flip character, to disperse as a function of momentum, and to change through the ferromagnetic transition temperature. Given the versatility of van der Waals materials, these excitons hold promise for new types of magneto-optical functionality.

I. INTRODUCTION

Excitons play a key role in determining the optical properties of solids, and their strong light-matter coupling paves the way for exploring new aspects of many-body physics [1]. Dark excitons are particularly interesting because they involve optical-dipole-forbidden transitions [2]. For this reason, they have reduced rates of radiative recombination and enhanced lifetimes and in many cases they can be sensitively controlled by external means, such as magnetic field [3]. These properties endow them with great potential in quantum information storage and communication [4].

Early studies of dark excitons began in the 1990s with quantum dots [5], followed by research on organic materials [6], and later expanded to transition-metal dichalcogenides [7]. The recent discovery of magnetic van der Waals (vdW) materials provides a new platform for studying excitons [8–12] and fascinating interactions between magnetism and excitons have been observed in several antiferromagnetic systems [13–17]. Understanding the electronic structure of these excitons and their interactions with magnetism is not only interesting from a fundamental point of view, but it may also offer new types of magneto-optical functionality such as optical read-out of magnetic states or quantum sensors [18]. CrI₃ pro-

vides an opportunity to study excitons in a ferromagnetic (FM) vdW material even down to the monolayer limit [19, 20]. Optical studies have revealed several bright excitons around 1.50, 1.85 and 2.2 eV in this material alongside several other optical features [20–23]; however dark excitons have not been definitively identified.

Resonant inelastic x-ray scattering (RIXS) is directly sensitive to optically forbidden excitations and has recently emerged as a powerful probe of excitons and their interactions with magnetism, in several magnetic vdW materials [13, 15–17, 24, 25]. In this Letter, we use Cr *L*₃-edge RIXS to identify two dark excitons near 1.7 eV in CrI₃. Both dark excitons are much sharper than other bright excitons and disperse with a bandwidth (~ 10 meV) similar to the energy scale of magnetic exchange interactions in this material. Together with the change of their intensities across the FM ordering temperature T_c , our experimental findings suggest an intimate relationship between CrI₃'s dark excitons and its magnetism. The electronic character of the dark excitons is borne out by our exact diagonalization (ED) calculations, which reveal that these excitons are spin-flip transitions in nature and are predominantly governed by Hund's coupling.

II. METHODS

Bulk single crystals of CrI₃ were synthesized by reacting the elements together in an evacuated fused silica ampoule [26]. CrI₃ undergoes a structural phase transition between the high-temperature monoclinic structure (space group *C*2/*m*, #12) and the low-temperature

* Current address: Stanford Institute for Materials and Energy Sciences, SLAC National Accelerator Laboratory, Menlo Park, CA 94025, USA; weihe@stanford.edu

† mdean@bnl.gov

rhombohedral structure (space group $R\bar{3}$, #148) over a broad temperature range (100–220 K) upon thermal cycling. The temperature of the sample was kept at $T = 30$ K, deep into the FM phase of the material, unless otherwise specified. We consequently used the rhombohedral unit cell notation with lattice parameters $a = b = 6.867$ Å, $c = 19.807$ Å, and $\gamma = 120^\circ$ throughout the manuscript, and index reciprocal space in terms of scattering vector $\mathbf{Q} = (H, K, L)$ in reciprocal lattice units (r.l.u.).

To avoid sample degradation in air, we mounted the sample on a copper sample holder in a glove box, cleaved with scotch tape in N_2 atmosphere ($\sim 3\%$ relative humidity level) to expose a fresh surface, and directly transferred the cleaved sample into the RIXS sample chamber. The surface normal of the sample was parallel to the c -axis. The in-plane orientation was determined by checking the residue on the scotch tape with a laboratory single-crystal x-ray diffractometer.

Cr L_3 -edge RIXS measurements were performed at the SIX 2-ID beamline of the National Synchrotron Light Source II. Data were taken with linear horizontal (π) polarization in the (HOL) scattering plane unless otherwise specified. The spectrometer was operated with a high energy resolution of 30.5 meV full-width at half-maximum (FWHM) (the exit slit size was 30 μm). Since the interlayer coupling in CrI_3 is weak, we fixed the scattering angle at $2\Theta = 150^\circ$ and expressed \mathbf{Q} in terms of the projected in-plane component of the momentum H . An angle-dependent self-absorption correction [27] was applied to the RIXS spectra, which, however, does not affect exciton energies or relative intensity changes at fixed \mathbf{Q} . The x-ray absorption spectroscopy (XAS) spectra were taken using the partial fluorescence yield mode with the RIXS detector, which covers the energy loss up to ~ 11 eV. The exit slit size was much larger (300 μm) for the XAS measurements to increase the flux.

III. IDENTIFICATION OF DARK EXCITONS

Figure 1(a) shows Cr L_3 -edge RIXS spectra of CrI_3 as a function of incident x-ray energy. Peaks below 2.5 eV energy loss are mainly local transitions within the Cr $3d$ orbital manifold, while broad features at higher energy can be ascribed to charge transfer processes that heavily involve ligand orbitals, and x-ray fluorescence arising from more extended states [29]. In the 1–3 eV energy window depicted in Fig. 1(b), three peaks, located at 1.50 eV, 1.88 eV, and 2.21 eV, match the exciton energies previously reported in optical experiments [20–23], so we denote them as bright excitons B1–B3. More excitingly, two additional features are observed at 1.66 eV and 1.71 eV, which were not seen in prior RIXS measurements due to their lower resolution (180/350 meV used to 30.5 meV used here [30, 31]). These modes have not yet been definitively identified in optical spectra, so, following standard terminology in optics, we will refer to

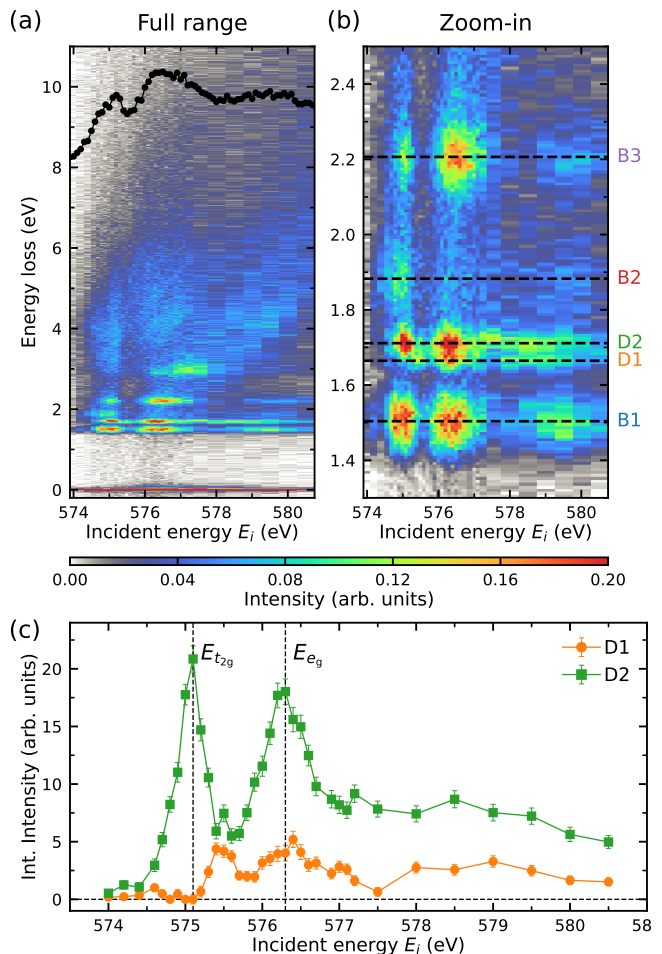


FIG. 1. Resonance behavior of dark excitons. (a) Cr L_3 -edge RIXS incident energy map taken at $T = 30$ K with π -polarized x-rays incident on the sample at $\theta = 14.5^\circ$ and scattered to $2\Theta = 150^\circ$ in the (HOL) scattering plane, corresponding to $H = -0.46$ r.l.u. The overlaid black curve on the top is XAS spectrum taken at the same conditions (including x-ray polarization, experimental geometry, and temperature). (b) Zoom of the exciton resonances. Horizontal dashed lines are fitted exciton energies. Two peaks near 1.7 eV are identified as the dark excitons and denoted as D1 and D2. The other three peaks are bright excitons previously observed in optical measurements [20–23] and therefore denoted as B1–B3. (c) The fitted integrated intensities of the two dark excitons as a function of incident photon energy E_i through the $E_{t_{2g}}$ and E_{e_g} resonances. D1 resonates at E_{e_g} , whereas D2 resonates at E_{e_g} and $E_{t_{2g}}$. As shown in Supplemental Material Sec. S1, these effects show minimal dichroism [28].

these as dark excitons and denote them as D1 and D2. We note that there are no additional features at energies below B1, contrary to an earlier prediction that the lowest energy dark excitons should exist around 0.9 eV [32].

Figure 1(b) exhibits two prominent resonances at $E_i = 575.1$ eV and 576.3 eV. Although there is strong t_{2g} - e_g mixing in CrI_3 , these two resonances correspond to more

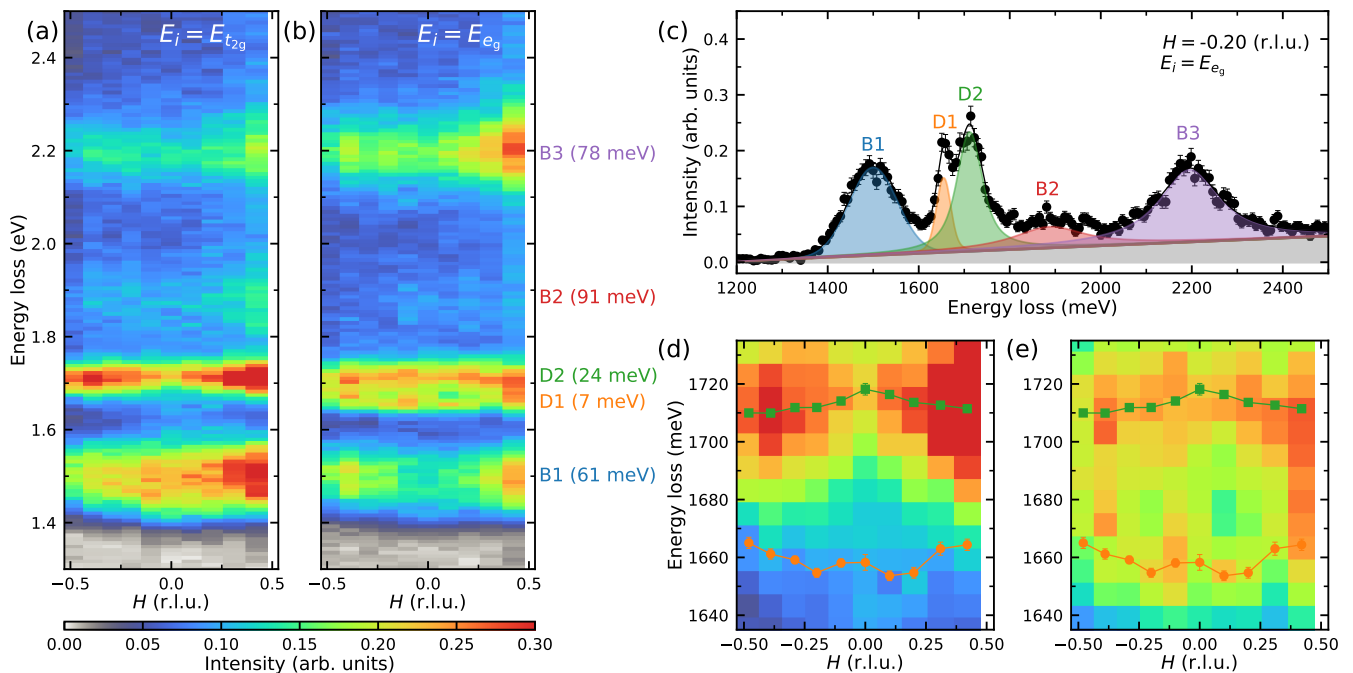


FIG. 2. Dispersion of the dark excitons. (a),(b) RIXS intensity map at $T = 30$ K as a function of in-plane momentum transfer H measured with (a) $E_i = E_{t_{2g}}$ where the D2 exciton is strongest and (b) $E_i = E_{e_g}$ where the D1 and D2 excitons are visible. The two dark excitons are much narrower than the other bright excitons, as seen by inspecting the intrinsic resolution deconvolved HWHM of the peaks as included in brackets after the peak labels. (c) Representative fit at $H = -0.20$ r.l.u. with $E_i = E_{e_g}$. (d),(e) Zoom of the dark exciton dispersion at (d) $E_i = E_{t_{2g}}$ and (e) $E_i = E_{e_g}$. For each momentum, we co-fit the spectra taken at the two resonances with shared exciton energies and widths. The co-fitted energy dispersion overlays the colormaps.

t_{2g} -like and more e_g -like orbital manifolds, respectively, as shown in Supplemental Fig. S16. We therefore label them as $E_{t_{2g}}$ and E_{e_g} resonances hereafter. As shown in Fig. 1(c), D2 resonates with t_{2g} and e_g intermediate states, but D1 only resonates at the e_g condition. An additional small resonance is present around 575.5 eV, which is generated by the exchange part of the core-valence Coulomb interaction on the Cr site. We will use the excitons' energy and angular dependence to identify their electronic character later in this Article.

IV. DARK EXCITONS DISPERSION

Having identified the existence of dark excitons in CrI_3 , we explore their propagation by mapping out their in-plane dispersion at the two resonant energies $E_{t_{2g}}$ and E_{e_g} , as presented in Fig. 2(a) and (b). Intriguingly, both excitons D1 and D2 exhibit a small dispersion but with opposite trends. We co-fit the spectra at the two different resonances, as described in Supplemental Material Sec. S3, and shown in Fig. 2(c). The fitted exciton energies in Fig. 2(d)&(e) confirm the presence of dispersion with similar bandwidths of ~ 10 meV. Such bandwidths are comparable to the energy scale of the magnon dispersion [33], hinting at the involvement of exciton-magnon interactions when these dark excitons propagate in the

lattice. The widths of the two dark excitons are dramatically sharper than those of other bright excitons, especially D1, which is almost resolution limited and about ten times narrower than the bright excitons [see Fig. 2(b)]. The three bright excitons do not exhibit any detectable dispersion (see Supplemental Fig. S9), likely due to their broader linewidths.

V. TEMPERATURE DEPENDENCE

Next, we measured the temperature dependence of RIXS spectra at $E_i = E_{t_{2g}}$ through the FM transition temperature $T_c = 61$ K up to room temperature. Figure 3 plots data and fits at two momenta. All excitons show an overall trend toward larger widths at higher temperatures. Such behavior is similar to RIXS measurements of excitons in other related materials such as NiPS_3 [13] and nickel dihalides [17, 24]. D2 (and to a lesser extent B3) shows a clear anomaly around the FM transition temperature T_c . The trends are even opposite through T_c at the two selected momenta, demonstrating an unusual momentum-dependent coupling between magnetism and dark exciton states. Other bright excitons, such as B1, also exhibit anomalies across T_c at certain momenta and incident energies (See Supplemental Fig. S3). The momentum dependence of these anomalies indicates under-

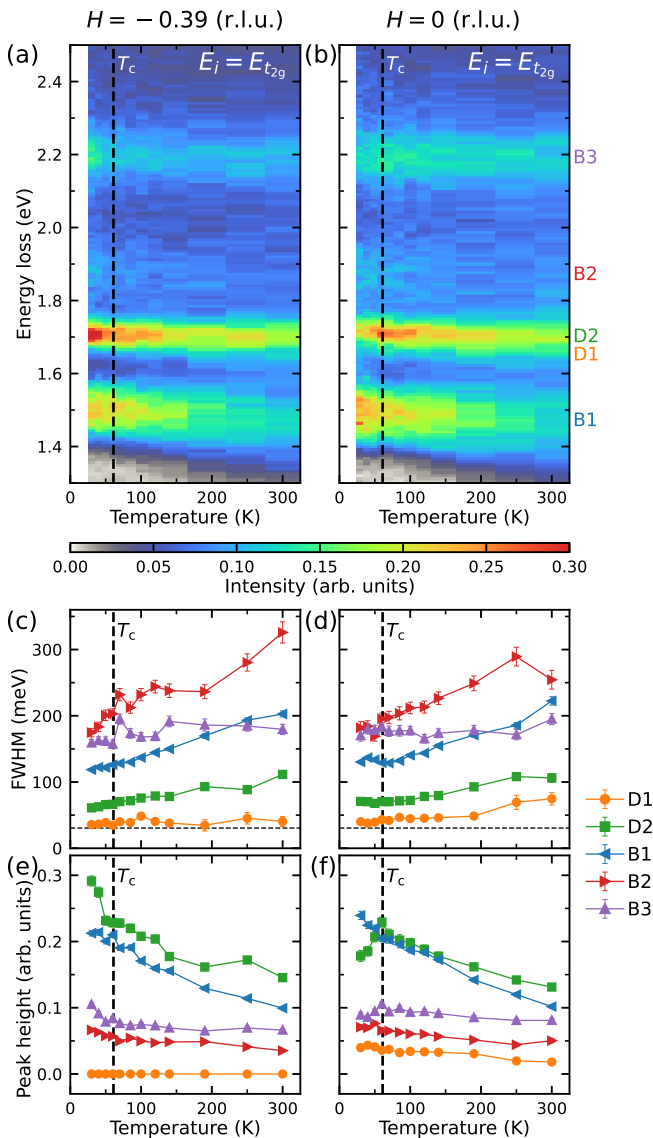


FIG. 3. Temperature dependence of the dark excitons. (a),(b) RIXS intensity map as a function of temperature measured at two different in-plane momenta ($H = -0.39$ and $H = 0$ r.l.u., respectively) with the same incident energy $E_{t_{2g}}$. (c)–(f) Corresponding FWHM and peak height extracted from the fits as a function of temperature. Changes in peak height through T_c primarily reflect changes in the integrated intensity of the peaks. We plot the peak intensity here because this quantity can be determined more precisely. Error bars represent one standard deviation. The fits were performed by co-fitting spectra taken at two incident energies with shared exciton energies and widths for each momentum and temperature. The data taken at the other incident energy E_{e_g} are shown in Supplemental Material Sec. S2 [28]. The vertical black lines indicate the FM transition temperature T_c and the horizontal black lines in (c)&(d) indicate the energy resolution.

lying physics that cannot be fully captured by established cluster-based methods commonly used to interpret RIXS. We also note that B1 (and to a lesser extent D2) softens steadily upon warming, particularly above T_c , which is reminiscent of the exciton behavior in NiPS_3 and NiI_2 [13, 24]. Such interesting behavior might be related to the electron-phonon interactions, which was used to explain the electronic gap shift observed in optics [34].

VI. ELECTRONIC CHARACTER OF EXCITONS

An advantage of RIXS compared to optics is that it couples directly to dipole-forbidden transitions in a well-known way, allowing us to extract the electronic character of the excitons. Indeed, ambiguities in the optical cross section for these excitons has led to different suggestions for the types of excitations present in chromium trihalides in 1.50–1.85 eV window including features coming from trigonal crystal fields to vibronic structures [21, 22]. To interpret the present spectra, we built an Anderson impurity model (AIM) for CrI_3 and computed the RIXS spectrum using ED methods [35]. The model includes Coulomb repulsion, Hund’s coupling, crystal field, and hopping terms derived from the Wannierization of our CrI_3 density functional theory (DFT) calculations as detailed in Appendix A. The spectra, shown in Fig. 4(a) and (b), capture the exciton energies including the double-peak structure of the two dark excitons and the overall trends in the resonances.

To identify the excitons, we report the final state expectation values of the spin-squared ($\langle \hat{S}^2 \rangle$) and electron population operators in Fig. 4(c)–(e). We note that it is vital to have a small charge-transfer energy (in fact, the best fit is achieved using $\Delta = -1.3$ eV with an error bar of ~ 1 eV) to obtain the correct energies for the entire spectrum. Such a small (or even slightly negative) charge transfer energy leads to approximately four electrons in the d states and approximately one hole occupying the ligand e_g orbitals not only in the ground states but also in the low energy excitations, as shown in Fig. 4(e), and in accordance with previous DFT-based results [32, 36–38]. The importance of charge-transfer is further underlined by the fact that a single-site atomic model cannot adequately fit the spectrum (see Supplemental Material Sec. 5A [28]). As such, the excitations observed here have substantial I character and are not strictly dd -excitations. The non-dispersive modes observed here are well-described by the broader concept of ligand-field excitons [39]. However, since these are by definition local, the dispersive D1 and D2 are, in our opinion, best termed as excitons, although all these terms share some similarities [40].

The ground state features half-filled t_{2g} orbitals, with $\langle \hat{S}^2 \rangle \approx 3.75$, corresponding to a high-spin configuration with $S = 3/2$. The D1 and D2 dark excitons involve only a small change in electron population, with the largest

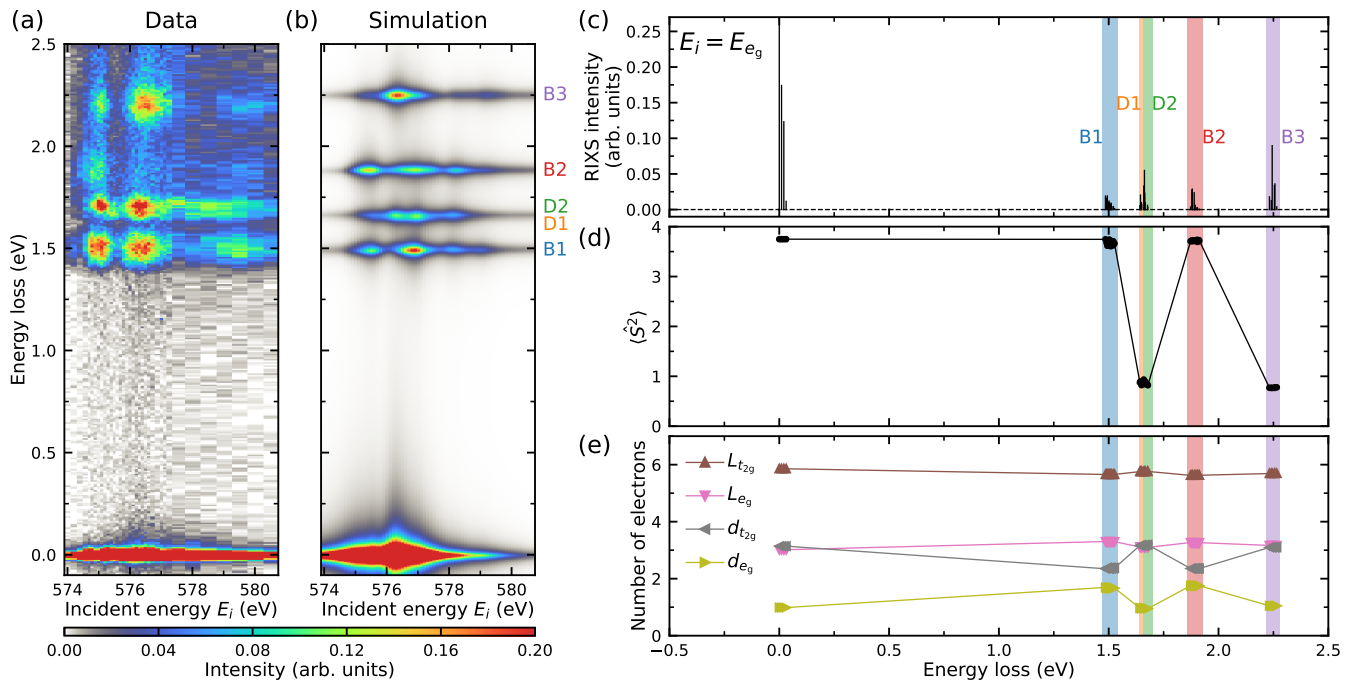


FIG. 4. Electronic character of the dark excitons. (a) RIXS intensity map as a function of incident photon energy through the Cr L_3 resonance. This is the same data presented in Fig. 1 with an energy window chosen to highlight the low-energy excitations. (b) RIXS calculations that reproduce the energy and resonant profile of the five lowest energy excitons in the material. (c) Calculated RIXS stick diagram at the main resonant energy E_{eg} . (d),(e) Analysis of the ground and excited states for the calculated RIXS spectrum. (d) Expectation value of the total spin operator squared $\langle \hat{S}^2 \rangle$. (e) Electron occupations of Cr $3d$ (denoted by d) and ligand (denoted by L) orbitals.

component of charge motion being about 0.1 electrons moving from the ligand $L_{t_{2g}}$ to the L_{e_g} states, the change from d to L states is even smaller at 0.03 electrons. More notable, this transition involves a low-spin configuration final state close to $S = 1/2$. Consequently, the energy scale of these dark excitons is determined mainly by the Hund's coupling for Cr $3d$ orbitals, consistent with their spin-flip character. Although D1 and D2 have dominant t_{2g} character, they feature non-zero mixing with the e_g manifold [see Fig. 4(e)]. This mixing endows D1 and D2 with a distinct orbital angular momentum, leading to their small energetic splitting and their distinct resonant profile at the t_{2g} and e_g conditions. The nearby bright excitons B1 and B2 are both crystal field transitions, conserving spin and moving an electron from the t_{2g} to the e_g states. Their energies are determined primarily by a combination of crystal field $10D_q$ and charge-transfer energy Δ (see Appendix A for the definitions of these quantities).

The higher-energy B3 exciton is again a spin-flip transition but with different symmetry that also redistributes a small amount of weight from the t_{2g} to e_g states. Its intensity exhibits a temperature dependence similar to that of the dark exciton D2 (although the change is less dramatic) in Fig. 3(e) and (f), possibly implying their similar spin-flip character. B3 is particularly broad, suggesting that this mode may be coupling to other exci-

tations. Such a coupling could play a role in the finite optical cross-section for this mode, which is larger than expected since it is a spin-flip transition. It is also possible that extended lattice models could be required to understand the detailed nature of the B2 and B3 excitons and their optical-cross section more fully, as suggested by many-body perturbation-theory plus Bethe-Salpeter equation calculations [32, 41].

VII. DISCUSSION AND CONCLUSIONS

The results here provide the first example of dispersive excitons in a FM vdW material, extending the recent identification of this phenomenon in antiferromagnetic vdW materials such as NiPS₃ [15] and nickel dihalides [17]. These dispersive excitons are all sharp spin-flip excitations bound by Hund's exchange interactions. The sharpness of the exciton (i.e., its long lifetime) may be related to its spin-flip nature because such transitions do not involve charge redistribution and therefore have minimal couplings to phonons and reduced efficiency of radiative recombination [20]. Prior works have made similar arguments for NiPS₃ and NiI₂, where the spin-flip character of excitons is regarded as the major aspect of their physics [13, 15, 42]. The small electron transfer involved in the transition has been suggested to play a minor role,

even though the magnitude of electron transfer in NiPS₃ is of order 0.2 electron and about seven times larger than the charge transfer observed here [15].

All these excitons also have appreciable ligand-hole involvement due to the small charge-transfer energy, which may facilitate the exciton propagation in the magnetic background [17]. However, there are also key distinctions between CrI₃ excitons and their counterparts in antiferromagnets. One clear difference is the exciton bandwidth. Phenomenologically, unlike the case in NiPS₃ or nickel dihalides where the exciton bandwidth is significantly smaller than the magnon bandwidth [15, 17], both dark excitons in CrI₃ have bandwidths comparable to the magnon bands [33]. In addition, these excitons exhibit a peculiar temperature dependence clearly correlated with T_c . Since CrI₃ exhibits layer-dependent magnetism [19], it would be of high interest to examine the exciton behaviors in the few-layer limit of CrI₃ in the near future. We also note that the energies of the CrI₃ dark excitons are higher than the electronic band gap, which was reported to be 1.1–1.3 eV [34] in CrI₃. This above-band-gap character may explain relatively large linewidth and their darkness in optics due to the strong sloping background coming from interband transitions. As a comparison, the previously discovered spin-flip excitons in NiPS₃ involve below-band-gap transitions [13, 15, 43].

In conclusion, we report two dark excitons in CrI₃ directly measured with high resolution RIXS. Our results showcase RIXS as a powerful tool in studying these dark states with a readily interpretable cross section and large momentum space coverage, complementary to optical measurements. The excitons feature strong coupling with the magnetism—they disperse with bandwidths similar to magnons and display unusual temperature dependence across the magnetic transition temperature. Our results will guide future optical experiments to detect and manipulate these dark excitons in CrI₃. In the past, various methods have been employed to brighten dark excitons in optical measurements, such as the application of an in-plane magnetic field [3], near-field coupling to surface plasmon polaritons [44], or by nano-optical tip-enhanced approaches [45]. With the better-targeted energies provided by our study, there is a high likelihood of probing these dark excitons in CrI₃ using these advanced optical techniques. Indeed, the possibility of accessing D1 and/or D2 optically is supported by a subset of the prior optical studies, which identified shoulder features in the spectra indicative of modes in the 1.7 eV range [20]. Moreover, our ED calculations will also inform future theory in more accurately describing the electronic properties of CrI₃. We believe that our discovery of dark excitons in CrI₃ is just the tip of the iceberg, and the utilization of RIXS will expedite the expansion of this family of materials and foster both the understanding of the fundamental physics and the potential applications of dark excitons in devices.

The supporting data for the plots in this article are openly available from the Zenodo database [46].

ACKNOWLEDGMENTS

Work performed at Brookhaven National Laboratory and Harvard University was supported by the U.S. Department of Energy (DOE), Division of Materials Science, under Contract No. DE-SC0012704. Work performed at the University of Texas at Austin was supported by the United States Army Research Office (W911NF-23-1-0394) (F.B.) and the National Science Foundation under the NSF CAREER award 2441874 (E.B.). F.B. acknowledges additional support from the Swiss NSF under fellowship P500PT.214437. S. J. was supported by the U.S. Department of Energy, Office of Science, Office of Basic Energy Sciences, under Award Number DE-SC0022311. Part of this research (T.B.) was conducted at the Center for Nanophase Materials Sciences, which is a DOE Office of Science User Facility. The work by J.W.V. is supported by the Quantum Science Center (QSC), a National Quantum Information Science Research Center of DOE. Crystal growth at ORNL as supported by the U.S. DOE, Office of Science, Basic Energy Sciences, Material Science and Engineering Division. This research used beamline 2-ID of the National Synchrotron Light Source II, a U.S. DOE Office of Science User Facility operated for the DOE Office of Science by Brookhaven National Laboratory under Contract No. DE-SC0012704. We also acknowledge glovebox resources made available through BNL/LDRD #19-013.

Appendix A: ED RIXS calculations

The RIXS spectra in this work were simulated based on standard ED methods implemented in the open source software EDRIXS [35]. The RIXS cross section was calculated using the Kramers-Heisenberg formula with the polarization-dependent dipole approximation. The model we employ here is an AIM, which was constructed using the bonding ligand orbitals of a CrI₆ cluster model. Here, we provide details on the parameters that we used and the methods that we employed to determine them.

In an AIM, we can represent a cluster with fewer orbitals by using symmetry-adapted linear combinations of ligand orbitals [47], making the calculation numerically much more efficient with essentially no loss of accuracy. In our case, we have 10 Cr 3*d* spin-orbitals and 10 ligand spin-orbitals with the same symmetry, so there are 13 electrons in total occupying 20 spin-resolved orbitals in the initial and final states. In the intermediate states, the Cr 2*p* orbitals are included to simulate the core hole created in the RIXS process. The calculations were performed in the full basis using the Fortran ED solver provided in EDRIXS [35]. For the RIXS cross section calculations, we have the experimental geometry explicitly considered, i.e., the scattering angle 2Θ is fixed to 150° and the sample angle θ is kept at 14.5°. An inverse core-hole lifetime $\Gamma_c = 0.3$ eV HWHM was used to fit the observed width of the resonance and the final state en-

ergy loss spectra are broadened using a Lorentzian function with a FWHM of 0.03 eV, in order to match the observed minimum width of the dark excitons.

The Hamiltonian of the model includes the Coulomb interactions, on-site energy for each orbital, hoppings between different orbitals, spin-orbit coupling, and the Zeeman interaction.

We parameterize the Coulomb interactions via Slater integrals, which include F_{dd}^0 , F_{dd}^2 , and F_{dd}^4 for the Cr 3d orbitals, and F_{dp}^0 , F_{dp}^2 , G_{dp}^1 , and G_{dp}^3 for the interactions between Cr 3d and 2p core orbitals in the intermediate states. F_{dd}^0 and F_{dp}^0 are related to the Cr 3d onsite Coulomb repulsion U_{dd} and core-hole potential U_{dp} , respectively, which are discussed later. The rest of the parameters are obtained by starting from their Hartree-Fock atomic values and scaling them down to account for the screening effect in the solids. For simplicity, we used two overall scaling factors, one for Cr 3d orbitals (k_{dd}) and the other for the core-hole interactions (k_{dp}).

Hopping integrals describe hybridization between different orbitals. This can be expressed using a 10×10

matrix H_{hopping} . We determined the off-diagonal inter-orbital hopping parameters from first-principles by calculating the electronic structure with the VASP DFT code [48, 49]. In this case, we used the Perdew-Burke-Ernzerhof (PBE) generalized gradient approximation [50] for the exchange-correlation functional without spin-orbit coupling. We employed projector augmented wave pseudopotentials [51, 52], considering Cr 3p electrons as valence (Cr_pv). The energy cutoff was set to 350 eV and we used a $15 \times 15 \times 15$ Monkhorst-Pack k -point mesh. We used an AMIX of 0.05 and a SIGMA smearing parameter of 0.05 eV. Finally, a tight-binding model is constructed using WANNIER90 [53–55]. We performed a Wannier projection of Cr 3d and I 5p orbitals without maximal localization. Disentanglement was omitted since these states form a well-isolated band set within the chosen energy window. The band structure from DFT calculations and the Wannier projected bands are shown in Fig. S12. The ligand orbitals were constructed from the appropriate linear combinations of the Wannier orbitals [46]. The hopping terms we obtained from this method are listed below (in units of eV).

$$H_{\text{hopping}} = \begin{matrix} & d_{3z^2-r^2} & d_{xz} & d_{yz} & d_{x^2-y^2} & d_{xy} & L_{3z^2-r^2} & L_{xz} & L_{yz} & L_{x^2-y^2} & L_{xy} \\ \begin{matrix} d_{3z^2-r^2} \\ d_{xz} \\ d_{yz} \\ d_{x^2-y^2} \\ d_{xy} \\ L_{3z^2-r^2} \\ L_{xz} \\ L_{yz} \\ L_{x^2-y^2} \\ L_{xy} \end{matrix} & \begin{pmatrix} -9.634 & 0.002 & 0.001 & 0 & -0.003 & -2.008 & -0.011 & -0.019 & -0.001 & 0.03 \\ 0.002 & -10.244 & 0.003 & 0.003 & 0.003 & -0.001 & -1.272 & -0.001 & 0.007 & -0.002 \\ 0.001 & 0.003 & -10.244 & -0.003 & 0.003 & 0.006 & -0.002 & -1.272 & -0.002 & -0.001 \\ 0.0 & 0.003 & -0.003 & -9.634 & 0 & 0.001 & -0.028 & 0.024 & -2.008 & 0.004 \\ -0.003 & 0.003 & 0.003 & 0 & -10.244 & 0.005 & -0.001 & -0.002 & -0.004 & -1.272 \\ -2.008 & -0.001 & 0.006 & 0.001 & -0.005 & 2.689 & 0.01 & 0.015 & 0.0 & -0.026 \\ -0.011 & -1.272 & -0.002 & -0.028 & -0.001 & 0.01 & 1.208 & -0.017 & 0.024 & -0.017 \\ -0.019 & -0.001 & -1.272 & 0.024 & -0.002 & 0.015 & -0.017 & 1.208 & -0.021 & -0.017 \\ -0.001 & 0.007 & -0.002 & -2.008 & -0.004 & 0.0 & 0.024 & -0.021 & 2.689 & -0.003 \\ 0.03 & -0.002 & -0.001 & 0.004 & -1.272 & -0.026 & -0.017 & -0.017 & -0.003 & 1.208 \end{pmatrix} \end{matrix} \quad (\text{A1})$$

Since hopping depends on how electronic wavefunctions are spread between different atoms, it is only weakly influenced by strongly correlated physics and DFT generally captures the magnitude of hopping quite accurately. For this reason, we consider the off-diagonal inter-orbital hopping values fixed to the quoted DFT-derived values. The on-site energies correspond to the diagonal elements in the hopping matrix H_{hopping} above. These on-site energies for the Cr 3d states are not easily obtainable from first principles because of the effects of strong correlations and the challenges in handling double-counting effects. We therefore consider the Cr 3d crystal field as a fitting parameter, which, in view of the approximately cubic symmetry of the Cr coordination, is specified by $10D_q$, which represents the splitting between the t_{2g} and e_g orbitals.

Since Coulomb interactions in the I 5p states are relatively weak and since the probability that these states are occupied by multiple holes is relatively low, the crystal field on the states is more accurately captured by DFT,

so to reduce the number of fitting parameters, we fix the ligand orbital crystal field $10D_q^L$ to the value extracted from our DFT results (1.481 eV). In this work, we define the charge-transfer, Δ , and Coulomb repulsion, U_{dd} , energies as the energy cost of specific transitions in the material with the Cr-ligand hopping switched off. U_{dd} reflects a $d_i^3 d_j^3 \rightarrow d_i^2 d_j^4$ transition and Δ is defined as the energy for a $d_i^3 \rightarrow d_i^4 \underline{L}$ transition, where i and j label Cr sites and \underline{L} denotes an iodine ligand hole. These energies include the effect of the Cr crystal field and represent the energies for a transition into the lowest-energy *ligand* orbital (rather than the center of the I p states). From a practical point of view, we perform our calculations varying the energy splitting of the Cr and ligand states and we subsequently determine Δ by diagonalizing the isolated Cr and ligand configurations and computing the appropriate differences in energy. The values of the diagonal elements in Eq. A1 are the final onsite energies determined for our model.

In the intermediate states with the presence of a core hole, we include a core-hole potential U_{dp} . U_{dd} is usually 4-6 eV in early transition metals and it is usually smaller when the charge transfer energy is small (which we will see is the case here), so we choose 4 eV [56, 57]. U_{dp} is only weakly dependent on solid state effects, so we choose a typical value of 6 eV.

The spin-orbit coupling terms for the Cr $3d$ orbitals (ζ_i and ζ_n for the initial and intermediate states, respectively) are weak and have negligible effects on the spectra. We consequently simply fixed them to their atomic values. Since we only measured RIXS energy map at the L_3 -edge, we also simply fixed the core-hole spin-orbit coupling parameter ζ_c to its atomic value.

A small Zeeman interaction term $g\mu_B\mathbf{B}\cdot\mathbf{S}$ was applied to the total spin angular momentum of the system, serving as the effective exchange field in the magnetically ordered state. We fixed $\mu_B B = 0.005$ eV to match the energy scale of the exchange interactions in CrI_3 [33].

In summary, we have four free parameters in our model, i.e., k_{dd} , k_{dp} , $10D_q$, and Δ . Most of these values are constrained by physical considerations. k_{dd} and k_{dp} quantify the screening. These are known to vary within a range of 0.5–0.9 from prior studies and these

values will typically also have reasonably similar values since both are affected by similar screening processes [58]. $10D_q$ in $3d$ octahedrally coordinated transition metal material ranges from about 0.5–3 eV and since iodine is relatively large size in ionic radius and relatively weakly electronegative, we expect a value in the lower half of this range. k_{dd} , k_{dp} , $10D_q$, and Δ have distinct effects on the RIXS energy map. k_{dd} directly scales the Hund's coupling and hence controls the energies of the dark excitons D1 and D2. The energies of the bright excitons B1 and B2 are primarily determined by both $10D_q$ and Δ . k_{dp} mainly affects the resonance profiles of these peaks. Thanks to the richly detailed spectra, the finite physically reasonable range of parameters, and the distinct effects of different parameters, we successfully obtained a well-constrained model with final parameters as $k_{dd} = 0.65$, $k_{dp} = 0.5$, $10D_q = 0.61$ eV, $\Delta = -1.3$ eV and verified that no other solutions exist. The level of agreement compares favorably with what can be expected for a model of this type accurately capturing the energy of the excitations while roughly capturing trends in peak intensities [13, 15, 17, 24]. The full list of parameters used in the model is shown in Tab. I. The estimated error bars are ~ 1 eV for all the Coulomb interactions and the charge-transfer energy Δ and ~ 0.2 eV for $10D_q$.

-
- [1] S. Koch, M. Kira, G. Khitrova, and H. Gibbs, Semiconductor excitons in new light, *Nature materials* **5**, 523 (2006).
- [2] W. R. Kitzmann, J. Moll, and K. Heinze, Spin-flip luminescence, *Photochem. Photobiol. Sci.* **21**, 1309 (2022).
- [3] X.-X. Zhang, T. Cao, Z. Lu, Y.-C. Lin, F. Zhang, Y. Wang, Z. Li, J. C. Hone, J. A. Robinson, D. Smirnov, S. G. Louie, and T. F. Heinz, Magnetic brightening and control of dark excitons in monolayer WSe_2 , *Nat. Nanotechnol.* **12**, 883 (2017).
- [4] E. Poem, Y. Kodriano, C. Tradonsky, N. H. Lindner, B. D. Gerardot, P. M. Petroff, and D. Gershoni, Accessing the dark exciton with light, *Nat. Phys.* **6**, 993 (2010).
- [5] M. Nirmal, D. J. Norris, M. Kuno, M. G. Bawendi, A. L. Efros, and M. Rosen, Observation of the “dark exciton” in CdSe quantum dots, *Phys. Rev. Lett.* **75**, 3728 (1995).
- [6] D. N. Congreve, J. Lee, N. J. Thompson, E. Hontz, S. R. Yost, P. D. Reusswig, M. E. Bahlke, S. Reineke, T. V. Voorhis, and M. A. Baldo, External quantum efficiency above 100% in a singlet-exciton-fission-based organic photovoltaic cell, *Science* **340**, 334 (2013).
- [7] G. Wang, A. Chernikov, M. M. Glazov, T. F. Heinz, X. Marie, T. Amand, and B. Urbaszek, Colloquium: Excitons in atomically thin transition metal dichalcogenides, *Rev. Mod. Phys.* **90**, 021001 (2018).
- [8] K. S. Burch, D. Mandrus, and J. G. Park, Magnetism in two-dimensional van der Waals materials, *Nature* **563**, 47 (2018).
- [9] C. Gong and X. Zhang, Two-dimensional magnetic crystals and emergent heterostructure devices, *Science* **363**, eaav4450 (2019).
- [10] Q. H. Wang, A. Bedoya-Pinto, M. Blei, A. H. Dismukes, A. Hamo, S. Jenkins, M. Koperski, Y. Liu, Q.-C. Sun, E. J. Telford, H. H. Kim, M. Augustin, U. Vool, J.-X. Yin, L. H. Li, A. Falin, C. R. Dean, F. Casanova, R. F. L. Evans, M. Chshiev, A. Mishchenko, C. Petrovic, R. He, L. Zhao, A. W. Tsen, B. D. Gerardot, M. Brotons-Gisbert, Z. Guguchia, X. Roy, S. Tongay, Z. Wang, M. Z. Hasan, J. Wrachtrup, A. Yacoby, A. Fert, S. Parkin, K. S. Novoselov, P. Dai, L. Balicas, and E. J. G. Santos, The magnetic genome of two-dimensional van der Waals materials, *ACS Nano* **16**, 6960 (2022).
- [11] Y. Ahn, X. Guo, S. Son, Z. Sun, and L. Zhao, Progress and prospects in two-dimensional magnetism of van der Waals materials, *Prog. Quant. Electron.* **93**, 100498 (2024).
- [12] K. F. Mak, J. Shan, and D. C. Ralph, Probing and controlling magnetic states in 2D layered magnetic materials, *Nature Reviews Physics* **1**, 646 (2019).
- [13] S. Kang, K. Kim, B. H. Kim, J. Kim, K. I. Sim, J. U. Lee, S. Lee, K. Park, S. Yun, T. Kim, A. Nag, A. Walters, M. Garcia-Fernandez, J. Li, L. Chapon, K. J. Zhou, Y. W. Son, J. H. Kim, H. Cheong, and J. G. Park, Coherent many-body exciton in van der Waals antiferromagnet NiPS_3 , *Nature* **583**, 785 (2020).
- [14] Y. J. Bae, J. Wang, A. Scheie, J. Xu, D. G. Chica, G. M. Diederich, J. Cenker, M. E. Ziebel, Y. Bai, H. Ren, C. R. Dean, M. Delor, X. Xu, X. Roy, A. D. Kent, and X. Zhu, Exciton-coupled coherent magnons in a 2D semiconductor, *Nature* **609**, 282 (2022).
- [15] W. He, Y. Shen, K. Wohlfeld, J. Sears, J. Li, J. Pelliari, M. Walicki, S. Johnston, E. Baldini, V. Bisogni, M. Mitrano, and M. P. M. Dean, Magnetically propagating Hund's exciton in van der Waals antiferromagnet

TABLE I. **Full list of parameters used in the AIM calculations.** (Except for the hopping integrals, which are provided in Eq. A1.) $F_{dd,i}$ and $F_{dd,n}$ are for the initial and intermediate states, respectively. Units are eV.

$10D_q$	$10D_q^L$	Δ	U_{dd}	U_{dp}	$F_{dd,i}^2$	$F_{dd,i}^4$	$F_{dd,n}^2$	$F_{dd,n}^4$	F_{dp}^2	G_{dp}^1	G_{dp}^3	ζ_i	ζ_n	ζ_c
0.61	1.481	-1.3	4.0	6.0	7.005	4.391	7.537	4.726	3.263	2.394	1.361	0.035	0.047	5.667

- NiPS₃, *Nat. Commun.* **15**, 3496 (2024).
- [16] M. F. DiScala, D. Staros, A. de la Torre, A. Lopez, D. Wong, C. Schulz, M. Barkowiak, V. Bisogni, J. Pellicciari, B. Rubenstein, and K. W. Plumb, Elucidating the role of dimensionality on the electronic structure of the van der Waals antiferromagnet NiPS₃, *Adv. Phys. Res.* **3**, 2300096 (2024).
- [17] C. A. Occhialini, Y. Tseng, H. Elnaggar, Q. Song, M. Blei, S. A. Tongay, V. Bisogni, F. M. F. de Groot, J. Pellicciari, and R. Comin, Nature of excitons and their ligand-mediated delocalization in nickel dihalide charge-transfer insulators, *Phys. Rev. X* **14**, 031007 (2024).
- [18] N. P. Wilson, W. Yao, J. Shan, and X. Xu, Excitons and emergent quantum phenomena in stacked 2D semiconductors, *Nature* **599**, 383 (2021).
- [19] B. Huang, G. Clark, E. Navarro-Moratalla, D. R. Klein, R. Cheng, K. L. Seyler, D. Zhong, E. Schmidgall, M. A. McGuire, D. H. Cobden, W. Yao, D. Xiao, P. Jarillo-Herrero, and X. Xu, Layer-dependent ferromagnetism in a van der Waals crystal down to the monolayer limit, *Nature* **546**, 270 (2017).
- [20] W. Jin, H. H. Kim, Z. Ye, G. Ye, L. Rojas, X. Luo, B. Yang, F. Yin, J. S. A. Horng, S. Tian, Y. Fu, G. Xu, H. Deng, H. Lei, A. W. Tsien, K. Sun, R. He, and L. Zhao, Observation of the polaronic character of excitons in a two-dimensional semiconducting magnet CrI₃, *Nat. Commun.* **11**, 4780 (2020).
- [21] I. Pollini and G. Spinolo, Intrinsic optical properties of CrCl₃, *physica status solidi (b)* **41**, 691 (1970).
- [22] V. M. Bermudez and D. S. McClure, Spectroscopic studies of the two-dimensional magnetic insulators chromium trichloride and chromium tribromide—I, *Journal of Physics and Chemistry of Solids* **40**, 129 (1979).
- [23] K. L. Seyler, D. Zhong, D. R. Klein, S. Gao, X. Zhang, B. Huang, E. Navarro-Moratalla, L. Yang, D. H. Cobden, M. A. McGuire, W. Yao, D. Xiao, P. Jarillo-Herrero, and X. Xu, Ligand-field helical luminescence in a 2D ferromagnetic insulator, *Nat. Phys.* **14**, 277 (2018).
- [24] S. Son, Y. Lee, J. H. Kim, B. H. Kim, C. Kim, W. Na, H. Ju, S. Park, A. Nag, K.-J. Zhou, Y.-W. Son, H. Kim, W.-S. Noh, J.-H. Park, J. S. Lee, H. Cheong, J. H. Kim, and J.-G. Park, Multiferroic-enabled magnetic-excitons in 2d quantum-entangled van der Waals antiferromagnet nli2, *Advanced Materials* **34**, 2109144 (2022).
- [25] M. Mitrano, S. Johnston, Y.-J. Kim, and M. P. M. Dean, Exploring quantum materials with resonant inelastic x-ray scattering, *Phys. Rev. X* **14**, 040501 (2024).
- [26] M. A. McGuire, H. Dixit, V. R. Cooper, and B. C. Sales, Coupling of Crystal Structure and Magnetism in the Layered, Ferromagnetic Insulator CrI₃, *Chem. Mater.* **27**, 612 (2015).
- [27] H. Miao, J. Lorenzana, G. Seibold, Y. Y. Peng, A. Amorese, F. Yakhov-Harris, K. Kummer, N. B. Brookes, R. M. Konik, V. Thampy, G. D. Gu, G. Ghiringhelli, L. Braicovich, and M. P. M. Dean, High-temperature charge density wave correlations in La_{1.875}Ba_{0.125}CuO₄ without spin-charge locking, *Proc. Natl. Acad. Sci. U.S.A.* **114**, 12430 (2017).
- [28] See Supplemental Material at [URL will be inserted by publisher] for further details of the calculations and fittings.
- [29] L. J. Ament, M. Van Veenendaal, T. P. Devereaux, J. P. Hill, and J. Van Den Brink, Resonant inelastic x-ray scattering studies of elementary excitations, *Rev. Mod. Phys.* **83**, 705 (2011).
- [30] A. Ghosh, H. J. M. Jönsson, D. J. Mukkattukavil, Y. Kvashnin, D. Phuyal, P. Thunström, M. Agåker, A. Nicolaou, M. Jonak, R. Klingeler, M. V. Kamalakar, T. Sarkar, A. N. Vasiliev, S. M. Butorin, O. Eriksson, and M. Abdel-Hafiez, Magnetic circular dichroism in the *dd* excitation in the van der Waals magnet CrI₃ probed by resonant inelastic x-ray scattering, *Phys. Rev. B* **107**, 115148 (2023).
- [31] Y. C. Shao, B. Karki, W. Huang, X. Feng, G. Sumanasekera, J.-H. Guo, Y.-D. Chuang, and B. Freelon, Spectroscopic Determination of Key Energy Scales for the Base Hamiltonian of Chromium Trihalides, *J. Phys. Chem. Lett.* **12**, 724 (2021).
- [32] M. Wu, Z. Li, T. Cao, and S. G. Louie, Physical origin of giant excitonic and magneto-optical responses in two-dimensional ferromagnetic insulators, *Nat. Commun.* **10**, 2371 (2019).
- [33] L. Chen, J.-H. Chung, B. Gao, T. Chen, M. B. Stone, A. I. Kolesnikov, Q. Huang, and P. Dai, Topological Spin Excitations in Honeycomb Ferromagnet CrI₃, *Phys. Rev. X* **8**, 041028 (2018).
- [34] L. Tomarchio, S. Macis, L. Mosesso, L. T. Nguyen, A. Grilli, M. C. Guidi, R. J. Cava, and S. Lupi, Low energy electrodynamics of CrI₃ layered ferromagnet, *Sci Rep* **11**, 23405 (2021).
- [35] Y. L. Wang, G. Fabbris, M. P. Dean, and G. Kotliar, EDRIXS: An open source toolkit for simulating spectra of resonant inelastic x-ray scattering, *Comput. Phys. Commun.* **243**, 151 (2019).
- [36] I. V. Kashin, V. V. Mazurenko, M. I. Katsnelson, and A. N. Rudenko, Orbitaly-resolved ferromagnetism of monolayer CrI₃, *2D Mater.* **7**, 025036 (2020).
- [37] S. Acharya, D. Pashov, B. Cunningham, A. N. Rudenko, M. Rösner, M. Grüning, M. Van Schilfhaarde, and M. I. Katsnelson, Electronic structure of chromium trihalides beyond density functional theory, *Phys. Rev. B* **104**, 155109 (2021).
- [38] Y. O. Kvashnin, A. N. Rudenko, P. Thunström, M. Rösner, and M. I. Katsnelson, Dynamical correlations in single-layer CrI₃, *Phys. Rev. B* **105**, 205124 (2022).
- [39] C. J. Ballhausen, *Introduction to ligand field theory* (McGraw Hill Book Company, 1962).
- [40] See the supplemental Material Section S6 for more discussion of this issue.
- [41] S. Acharya, D. Pashov, A. N. Rudenko, M. Rösner,

- M. v. Schilfgaard, and M. I. Katsnelson, Real- and momentum-space description of the excitons in bulk and monolayer chromium tri-halides, *npj 2D Mater. Appl.* **6**, 1 (2022).
- [42] I. J. Hamad, C. S. Helman, L. O. Manuel, A. E. Feiguin, and A. A. Aligia, Singlet polaron theory of low-energy optical excitations in nips₃, *Phys. Rev. Lett.* **133**, 146502 (2024).
- [43] S. Y. Kim, T. Y. Kim, L. J. Sandilands, S. Sinn, M. C. Lee, J. Son, S. Lee, K. Y. Choi, W. Kim, B. G. Park, C. Jeon, H. D. Kim, C. H. Park, J. G. Park, S. J. Moon, and T. W. Noh, Charge-Spin Correlation in van der Waals Antiferromagnet NiPS₃, *Physical Review Letters* **120**, 136402 (2018).
- [44] Y. Zhou, G. Scuri, D. S. Wild, A. A. High, A. Dibos, L. A. Jauregui, C. Shu, K. De Greve, K. Pistunova, A. Y. Joe, T. Taniguchi, K. Watanabe, P. Kim, M. D. Lukin, and H. Park, Probing dark excitons in atomically thin semiconductors via near-field coupling to surface plasmon polaritons, *Nat. Nanotechnol.* **12**, 856 (2017).
- [45] K.-D. Park, T. Jiang, G. Clark, X. Xu, and M. B. Raschke, Radiative control of dark excitons at room temperature by nano-optical antenna-tip Purcell effect, *Nat. Nanotechnol.* **13**, 59 (2018).
- [46] W. He, J. Sears, F. Barantani, T. Kim, J. W. Villanova, T. Berlijn, M. Lajer, M. A. McGuire, J. Pelliari, V. Bisogni, S. Johnston, E. Baldini, M. Mitrano, and M. P. M. Dean, Respository for: Dispersive dark excitons in van der Waals ferromagnet CrI₃ (2024), to be assigned.
- [47] M. W. Haverkort, M. Zwierzycki, and O. K. Andersen, Multiplet ligand-field theory using Wannier orbitals, *Physical Review B* **85**, 165113 (2012).
- [48] G. Kresse and J. Furthmüller, Efficient iterative schemes for ab initio total-energy calculations using a plane-wave basis set, *Phys. Rev. B* **54**, 11169 (1996).
- [49] G. Kresse and J. Furthmüller, Efficiency of ab-initio total energy calculations for metals and semiconductors using a plane-wave basis set, *Computational Materials Science* **6**, 15 (1996).
- [50] J. P. Perdew, K. Burke, and M. Ernzerhof, Generalized gradient approximation made simple, *Phys. Rev. Lett.* **77**, 3865 (1996).
- [51] P. E. Blöchl, Projector augmented-wave method, *Phys. Rev. B* **50**, 17953 (1994).
- [52] G. Kresse and D. Joubert, From ultrasoft pseudopotentials to the projector augmented-wave method, *Phys. Rev. B* **59**, 1758 (1999).
- [53] A. A. Mostofi, J. R. Yates, G. Pizzi, Y.-S. Lee, I. Souza, D. Vanderbilt, and N. Marzari, An updated version of Wannier90: A tool for obtaining maximally-localised Wannier functions, *Computer Physics Communications* **185**, 2309 (2014).
- [54] N. Marzari and D. Vanderbilt, Maximally localized generalized Wannier functions for composite energy bands, *Phys. Rev. B* **56**, 12847 (1997).
- [55] I. Souza, N. Marzari, and D. Vanderbilt, Maximally localized Wannier functions for entangled energy bands, *Phys. Rev. B* **65**, 035109 (2001).
- [56] A. Bocquet, T. Saitoh, T. Mizokawa, and A. Fujimori, Systematics in the electronic structure of 3d transition-metal compounds, *Solid State Communications* **83**, 11 (1992).
- [57] S. Feldkemper and W. Weber, Generalized calculation of magnetic coupling constants for Mott-Hubbard insulators: Application to ferromagnetic Cr compounds, *Phys. Rev. B* **57**, 7755 (1998).
- [58] F. De Groot and A. Kotani, *Core level spectroscopy of solids* (CRC press, 2008).

Supplemental Material: Dispersive Dark Excitons in van der Waals Ferromagnet CrI₃

(Dated: January 17, 2025)

This document provides a resonant inelastic x-ray scattering (RIXS) energy map measured with linear vertical (σ) polarization, x-ray absorption spectroscopy (XAS) data, additional temperature dependence of RIXS spectra measured at E_{e_g} resonance, detailed description of the fitting procedures for the RIXS data with linecuts showing the fitting, plots showing integrated peak intensity temperature dependence, further details of our exact diagonalization (ED) calculations, and a discussion of terminology for the excitations studies here.

S1. ADDITIONAL RIXS ENERGY MAP WITH σ POLARIZATION AND XAS DATA

Besides the incident energy dependent RIXS intensity map measured with linear horizontal (π) polarization shown in the main text, we also collected data with linear vertical (σ) polarization as displayed in Fig. S1. All experimental parameters were kept the same for these two sets of measurements, with the only difference being the incident x-ray polarization. The two RIXS energy maps are very similar with nearly identical resonance behaviors, although the σ -channel data has slightly lower intensity. We therefore chose π -polarization for the following angular and temperature-dependent measurements to maximize the RIXS intensity. The XAS also exhibits a weak dichroism for the two polarizations, as shown in Fig. S2.

S2. ADDITIONAL TEMPERATURE DEPENDENCE OF RIXS SPECTRA AT E_{e_g} RESONANCE

Besides the temperature dependent RIXS intensity map measured at $E_{t_{2g}}$ resonance shown in the main text, we also have data collected at E_{e_g} resonance as displayed in Fig. S3. As described in detail in the next section, we co-fit these two data sets with shared exciton widths and energies. Just like the data at $E_{t_{2g}}$, the excitons also exhibit abrupt changes in peak height near the ferromagnetic (FM) transition temperature T_c at this resonance, although the changes are less dramatic.

S3. FITTING OF THE RIXS SPECTRA

A. Functional form

We fit RIXS spectra with five peaks plus a linear background to parameterize the excitons as a function of incident energy, momentum transfer, or temperatures. We used Voigt functions to fit the dark excitons D1–D2 and bright excitons B2–B3. The width of the Gaussian component was fixed to the energy resolution of 30.5 meV, which was determined by a reference measurement on a multilayer heterostructure sample with a strong elastic scattering signal. The bright exciton B1 is better described by a Gaussian lineshape. We found that these simple lineshapes provide a satisfactory fit to the spectra.

To obtain high-precision values for the exciton energies, we carefully calibrated the energy zero of the spectra. In the low-energy region of the spectra, we identified one prominent elastic peak along with a weak magnon feature in the tail of peak. We used a Gaussian function with its width fixed to the energy resolution to fit the elastic peak. For the magnon, we chose a damped harmonic oscillator (DHO) function below and convoluted this function with a Gaussian resolution function to model it. The form of the DHO function we used is:

$$S(\mathbf{Q}, \omega) = \frac{\omega \chi_Q}{1 - \exp(-\omega/k_B T)} \cdot \frac{2z_Q f_Q}{(\omega^2 - f_Q^2)^2 + (\omega z_Q)^2} \quad (1)$$

where f_Q is the undamped energy, χ_Q is the oscillator strength, z_Q is the damping factor, k_B is the Boltzmann constant, and T is temperature. Because the elastic peak dominates the spectral weight in this region, the inclusion of the magnon peak in the fitting function has minimal effect on the fitted elastic peak position. The error bars for the fitted exciton peak positions shown in Fig. 2 include not only their own fitting errors but also the fitting errors of the energy zero.

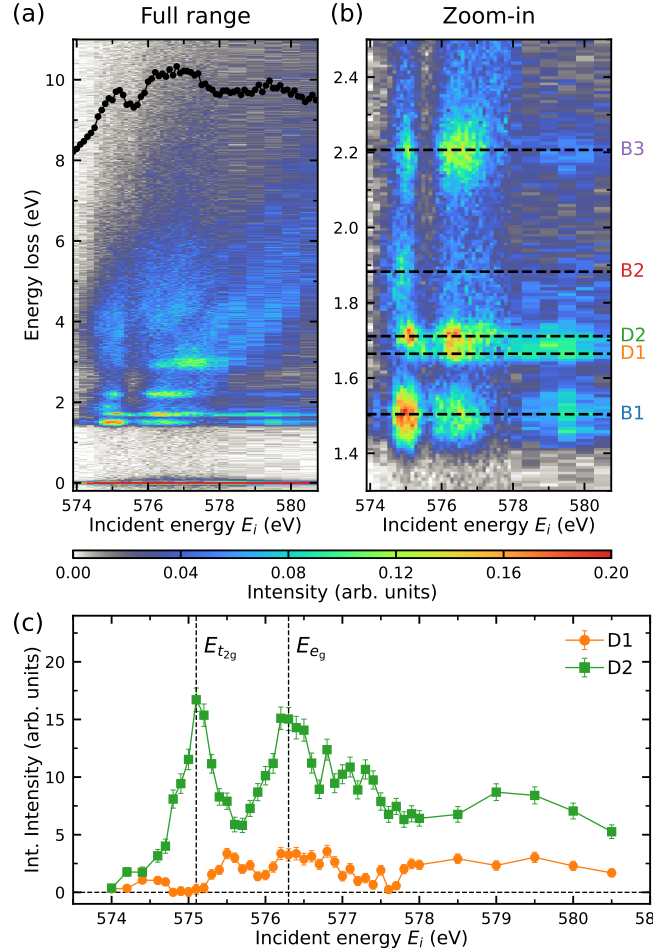


FIG. S1. Additional resonance behavior of dark excitons measured with linear vertical (σ) polarization. (a) Incident photon energy E_i dependence of the RIXS intensity map at the Cr L_3 -edge with σ -polarized incident x-rays. The measurement was taken at $T = 30$ K with x-rays incident on the sample at $\theta = 14.5^\circ$ and scattered to $2\Theta = 150^\circ$ in the (HOL) scattering plane. The overlaid black curve on the top is XAS spectrum taken at the same conditions (including x-ray polarization, experimental geometry, and temperature). (b) Zoom-in of the RIXS energy map in the vicinity of the dark excitons. Horizontal dashed lines are fitted exciton energies. (c) The fitted integrated intensities of the two dark excitons as a function of incident photon energy E_i . Error bars represent one standard deviation. Similar to the π polarization data in the main text, both dark excitons reach their local maxima in intensity at E_{e_g} , while D1 has nearly zero spectral weight at $E_{t_{2g}}$.

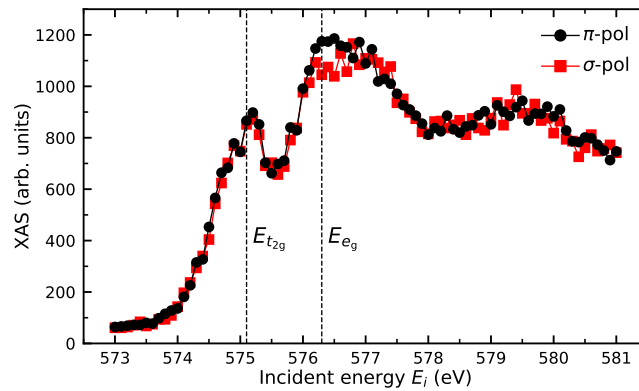


FIG. S2. XAS spectra with both linear horizontal (π) and linear vertical (σ) polarizations. The spectra were taken at $T = 30$ K. The sample geometry was the same as the measurement for the RIXS energy map (i.e., $\theta = 14.5^\circ$, $2\Theta = 150^\circ$, (HOL) scattering plane) but with a much larger exit slit size of $300 \mu\text{m}$. The vertical dashed lines label the two resonant energies. This is the same data shown in Figs. 1 and S1 and provided here to show the comparison between the two polarizations.

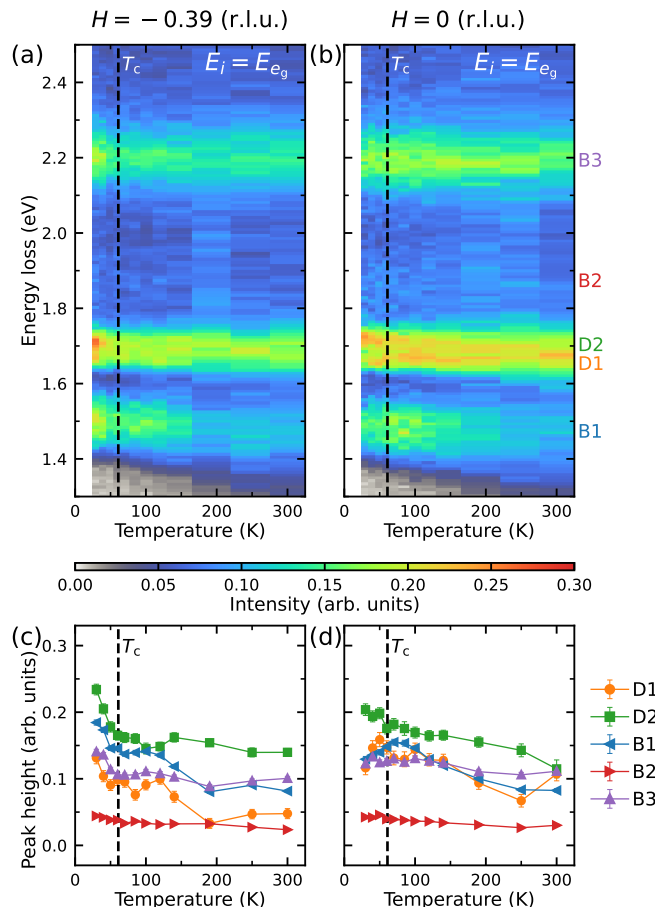


FIG. S3. Additional temperature dependence of the dark excitons at E_{e_g} resonance. (a),(b) RIXS intensity map as a function of temperature measured at two different in-plane momenta ($H = -0.39$ and $H = 0$ r.l.u., respectively) with the same incident energy E_{e_g} . (c),(d) Corresponding peak height extracted from the fits as a function of temperature. Error bars represent one standard deviation. The dashed lines indicate the FM transition temperature T_c .

B. Incident energy dependence

As expected for a Raman-like RIXS process, the exciton energies and widths were found to be independent of incident energy, providing additional constraints in fitting the incident energy dependent RIXS spectra. Specifically, we first co-fitted all the spectra taken with π -polarization, applying the constraints that each exciton maintains the same position and width across all spectra (see Fig. S4). Then, we co-fitted all the spectra taken with σ -polarization. As shown in Fig. S5, we found that even when we forced the exciton positions and widths to match the fitted values obtained from the π -polarization data, the fits still look reasonably good, demonstrating the robustness of the fitting result.

C. In-plane momentum transfer dependence

For the fitting of the RIXS spectra at various in-plane momentum transfers, since we have measurements at two incident energies, we applied the above-mentioned co-fitting method and constrained the exciton energy and widths to be the same across both spectra. Such a co-fitting strategy with shared exciton positions and widths is particularly useful in obtaining consistent fits for the dark exciton D1, which has a minuscule spectral weight at $E_{t_{2g}}$ resonance. We present the best fits to the linecuts of the RIXS spectra in Fig. S6–S8. In Fig. S9, we show the fitted peak positions of the three bright excitons as a function of the in-plane momentum transfers. No clear dispersion is detected for these excitons beyond their error bars.

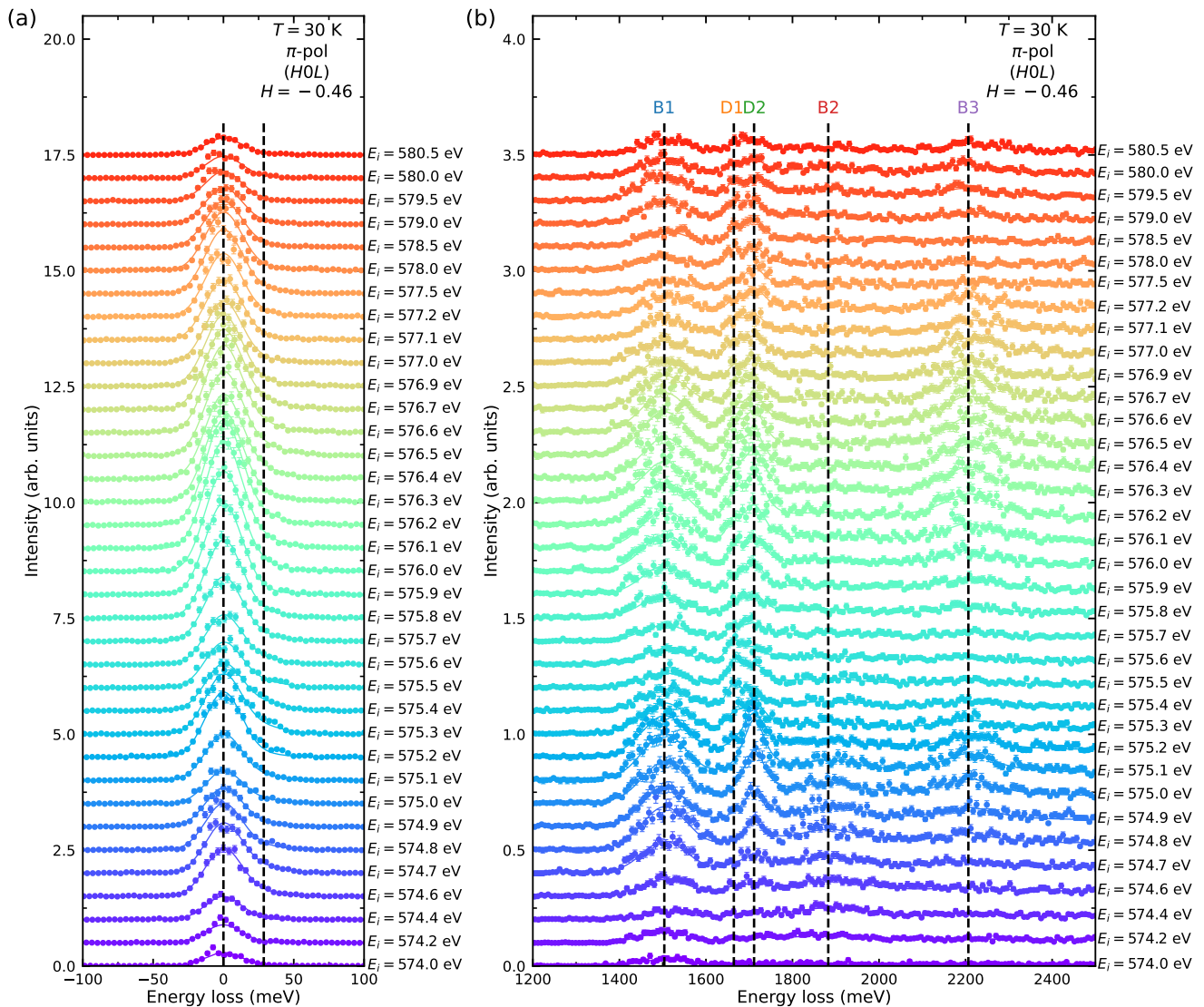


FIG. S4. RIXS spectra measured at various incident energies with linear-horizontally (π -) polarized x-rays. (a) RIXS spectra near the elastic line. (b) RIXS spectra in the energy window covering the excitons. The measurements were taken at various incident photon energy through the Cr L_3 -edge measured in the (HOL) plane at $T = 30$ K. These data are the same as the intensity maps shown in Fig. 1(a)–(b) and are provided to show the linecuts directly. Data are shifted vertically for clarity. The solid lines are the fits to the data. Error bars represent one standard deviation. Vertical black dashed lines label the exciton energies.

D. Temperature dependence

We used the same co-fitting approach to fit the temperature-dependent RIXS spectra. However, due to the broadening of the exciton peaks, not every spectrum yielded a converged fitting result. Therefore, we added additional constraints, including the integrated intensity of B2 at both resonance energies and the integrated intensity of D1 at the $E_{t_{2g}}$ resonance. We found that these quantities have minimal temperature dependence, so we fixed them to their respective average values obtained from the initial fits. The final best fits to the temperature-dependent RIXS spectra are shown in Fig. S10 and S11. Figure S12 displays the fitted peak positions of all five excitons as a function of temperature measured. B1 (and to a lesser extent D2) shows a clear red-shift upon warming. The red shift is less apparent for other excitons, partly due to their weak intensities and/or broad peak width.

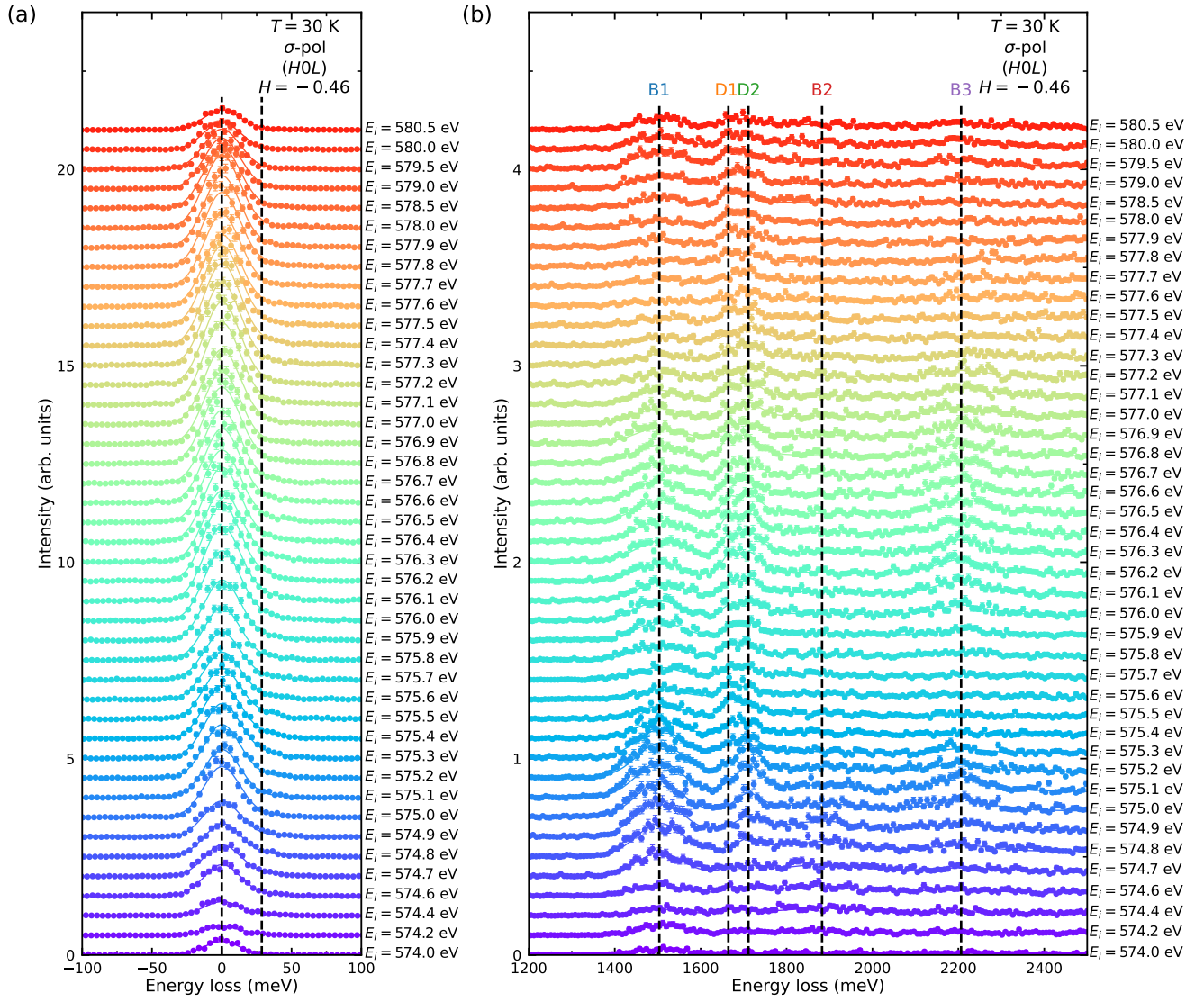


FIG. S5. RIXS spectra measured at various incident energies with linear-vertically (σ -) polarized x-rays. (a) RIXS spectra near the elastic line. (b) RIXS spectra in the energy window covering the excitons. The measurements were taken at various incident photon energy through the Cr L_3 -edge measured in the (H0L) plane at $T = 30$ K. These data are the same as the intensity maps shown in Fig. S1(a)–(b) and are provided to show the linecuts directly. Data are shifted vertically for clarity. The solid lines are the fits to the data. Error bars represent one standard deviation. Vertical black dashed lines label the exciton energies.

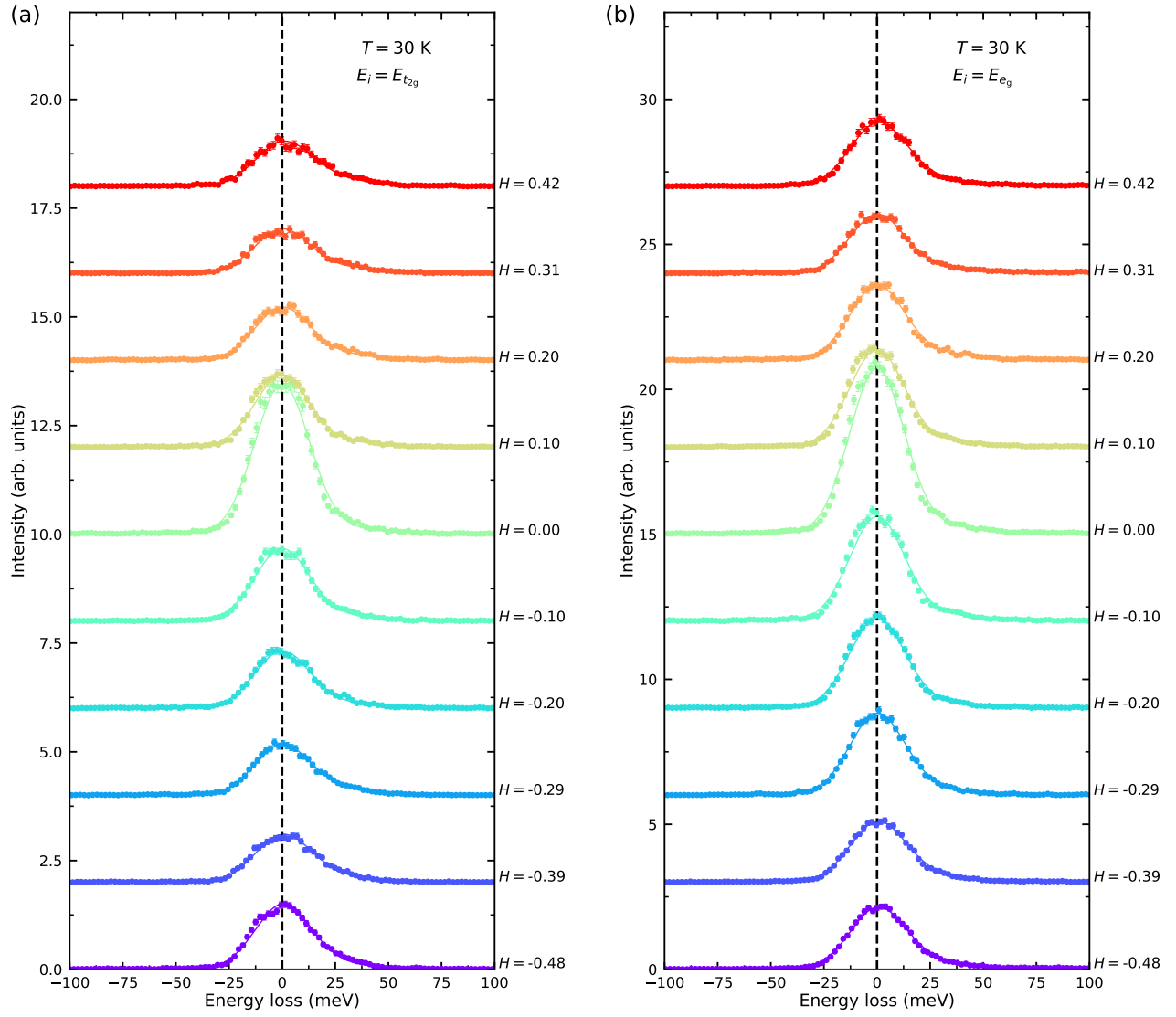


FIG. S6. RIXS spectra measured at various in-plane momentum transfer H with an energy window chosen to isolate the elastic line. (a) RIXS spectra at $E_{t_{2g}}$ resonance. (b) RIXS spectra at E_{e_g} resonance. The measurements were taken in the $(H0L)$ plane at $T = 30$ K with linear horizontal (π) polarization of the incident x-rays. Data are shifted vertically for clarity. The solid lines are the fits to the data. Error bars represent one standard deviation. Vertical black dashed lines label the energy zero.

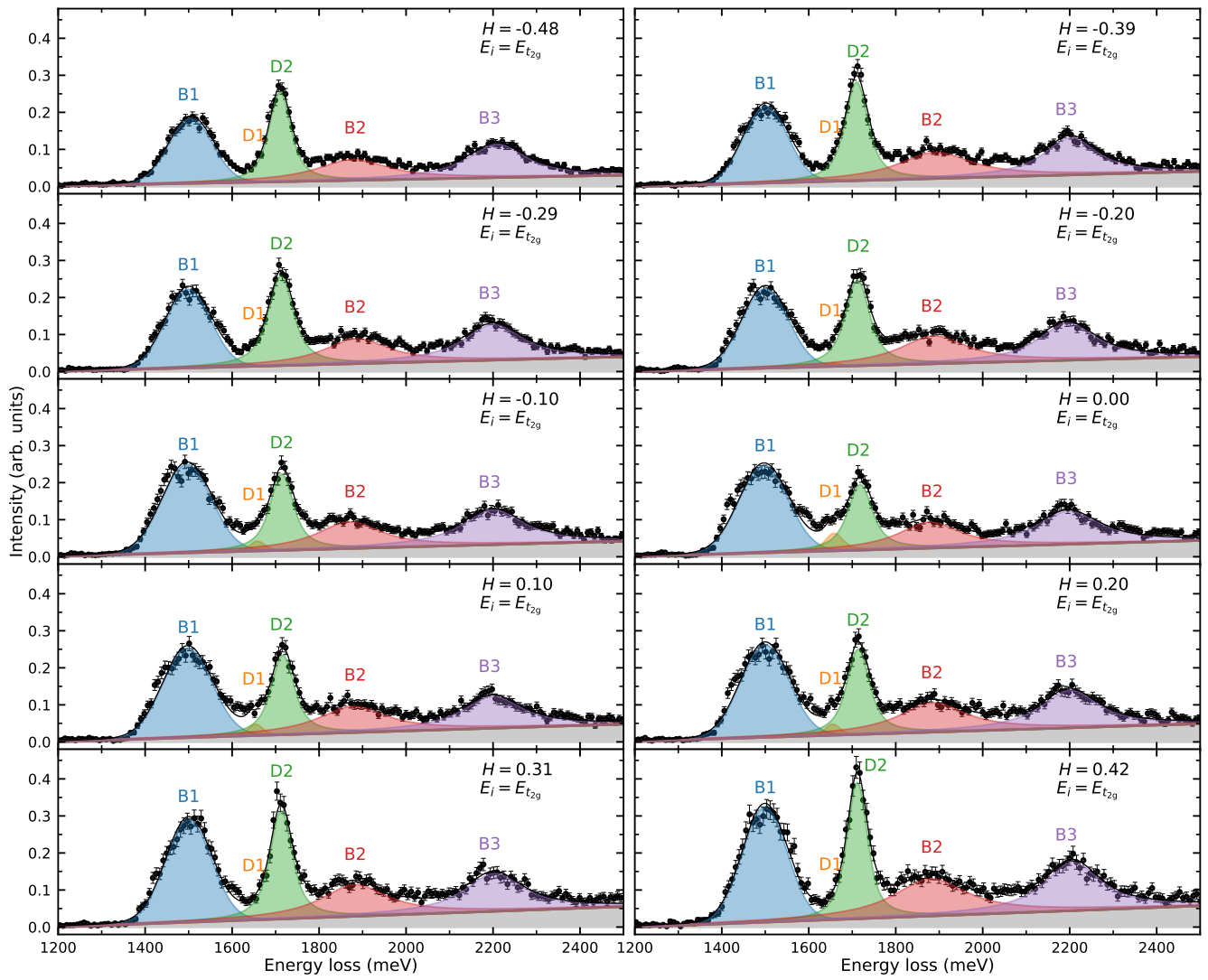


FIG. S7. RIXS spectra measured at various in-plane momentum transfer H at $E_{i_{2g}}$ resonance with an energy window chosen to isolate the excitons. The measurements were taken in the (HOL) plane at $T = 30$ K with linear horizontal (π) polarization of the incident x-rays. These data are the same as the intensity maps shown in Fig. 2(a) and are provided to show the linecuts directly. Solid black lines are the fits to the data, with shaded areas showing the contributions from different components. Error bars represent one standard deviation.

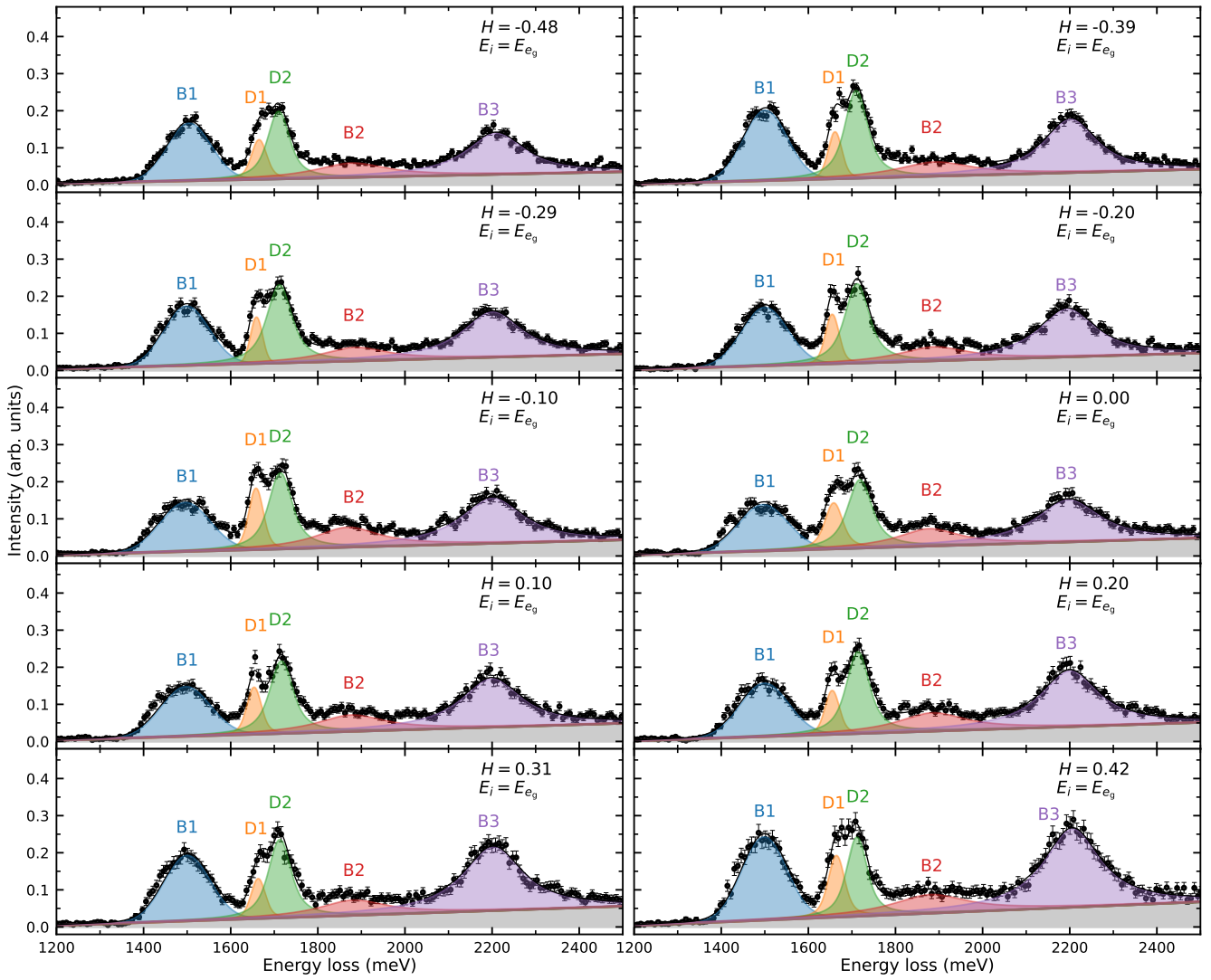


FIG. S8. RIXS spectra measured at various in-plane momentum transfer H at E_{eg} resonance with an energy window chosen to isolate the excitons. The measurements were taken in the $(H0L)$ plane at $T = 30$ K with linear horizontal (π) polarization of the incident x-rays. These data are the same as the intensity maps shown in Fig. 2(b) and are provided to show the linecuts directly. Solid black lines are the fits to the data, with shaded areas showing the contributions from different components. Error bars represent one standard deviation.

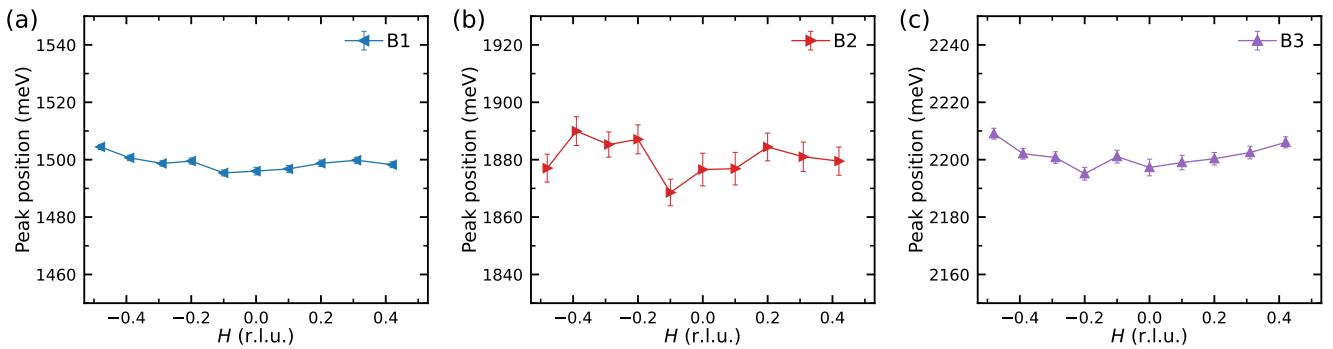


FIG. S9. The extracted momentum dependent energies of the three bright excitons. Error bars represent one standard deviation. No clear dispersion is detected for these bright excitons.

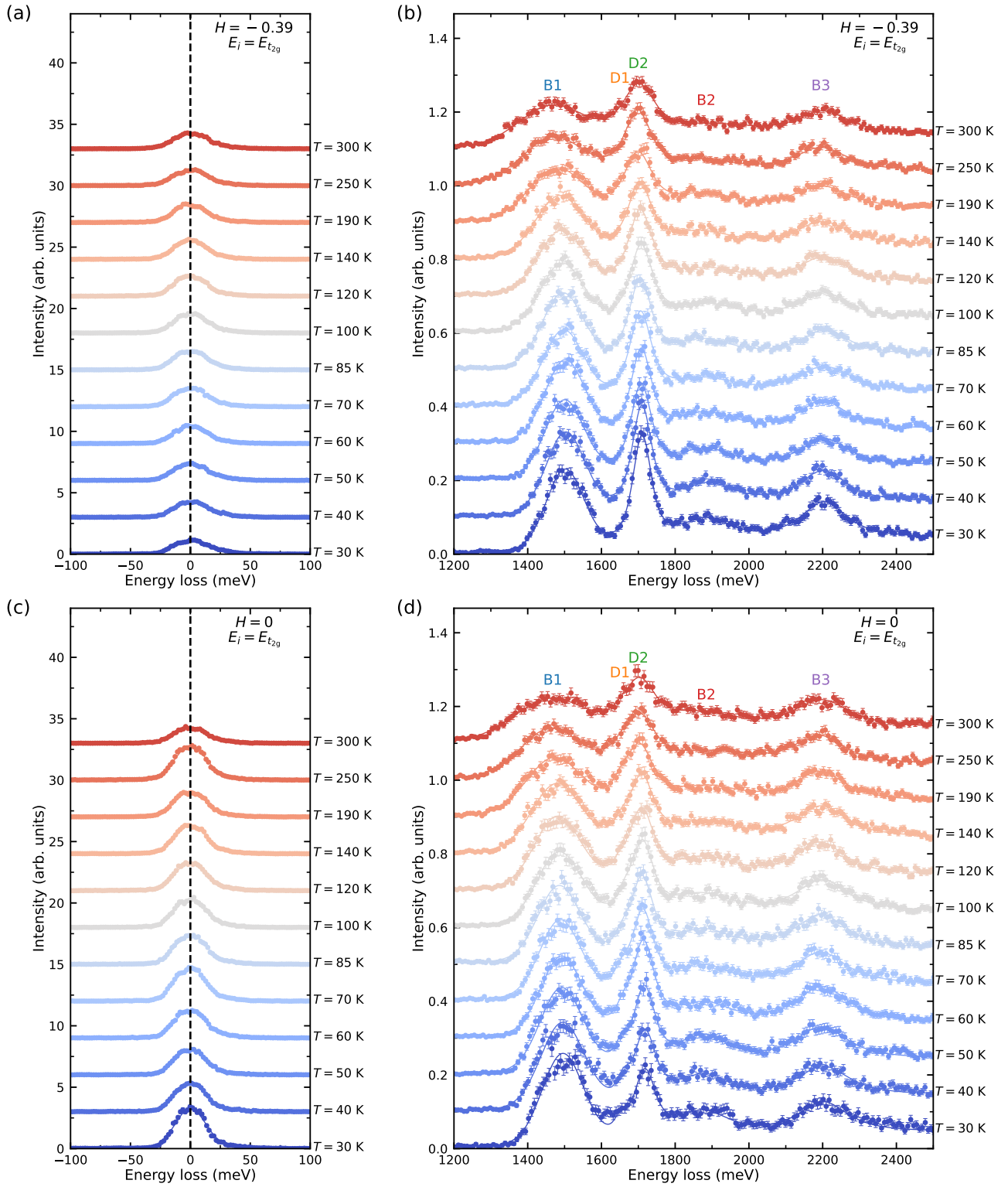


FIG. S10. RIXS spectra measured at various temperatures at $E_{t_{2g}}$ resonance. (a),(b) RIXS spectra taken at $H = -0.39$ r.l.u. with the energy window chosen to isolate the elastic line and excitons, respectively. (c),(d) RIXS spectra taken at $H = 0$ r.l.u. with the energy window chosen to isolate the elastic line and excitons, respectively. All the measurements were done with linear horizontal (π) polarization of the incident x-rays. These data are the same as the intensity maps shown in Fig. 3(a)–(b) and are provided to show the linecuts directly. Data are shifted vertically for clarity. The solid lines are the fits to the data. Error bars represent one standard deviation. Vertical dashed lines label the energy zero.

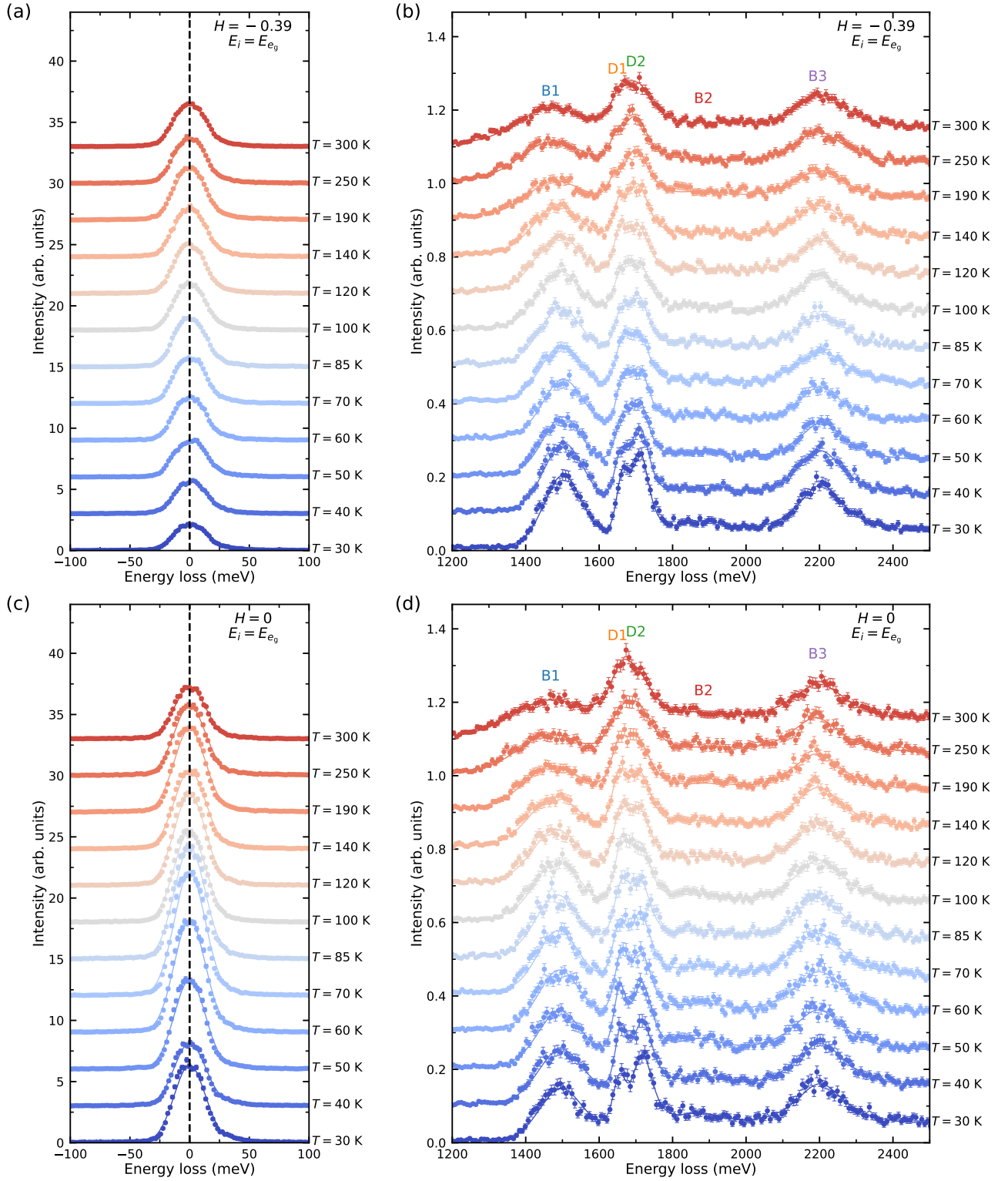


FIG. S11. RIXS spectra measured at various temperatures at E_{e_g} resonance. (a),(b) RIXS spectra taken at $H = -0.39$ r.l.u. with the energy window chosen to isolate the elastic line and excitons, respectively. (c),(d) RIXS spectra taken at $H = 0$ r.l.u. with the energy window chosen to isolate the elastic line and excitons, respectively. All the measurements were done with linear horizontal (π) polarization of the incident x-rays. These data are the same as the intensity maps shown in Fig. S3(a)–(b) and are provided to show the linecuts directly. Data are shifted vertically for clarity. The solid lines are the fits to the data. Error bars represent one standard deviation. Vertical dashed lines label the energy zero.

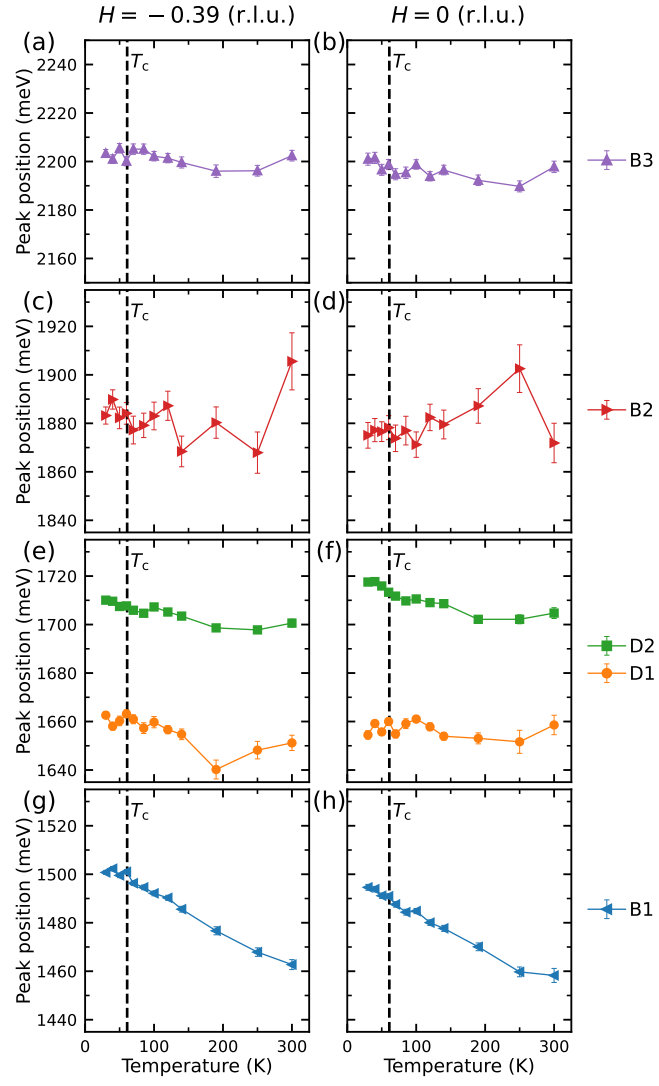


FIG. S12. The extracted temperature dependent energies of the excitons at two different in-plane momenta ($H = -0.39$ and $H = 0$ r.l.u.). Error bars represent one standard deviation. The dashed lines indicate the FM transition temperature T_c .

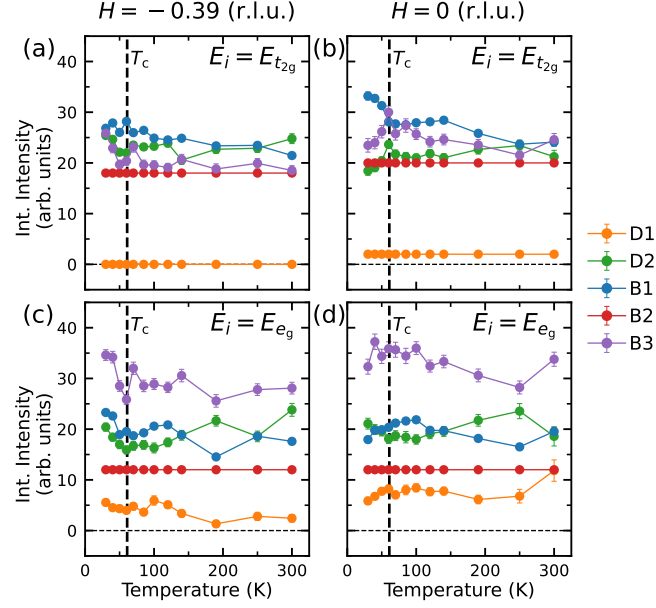


FIG. S13. Temperature dependence of the dark excitons at (a),(c) $H = -0.39$ r.l.u. and (b),(d) $H = 0$ at two different in-plane momenta ($H = -0.39$ and $H = 0$ r.l.u.). This re-plots the same data as in Fig. 3 of the main text and Fig. S3, but using integrated intensity rather than peak height. Error bars represent one standard deviation.

S4. INTEGRATED PEAK INTENSITY TEMPERATURE DEPENDENCE

For completeness, here in Fig. S13 we re-plot the same data provided in Fig. 3 of the main text and Fig. S3 in terms of integrated peak intensity rather than peak height. The anomalies across T_c are apparent in integrated peak intensity as well. This is because of the slow change in peak width below T_c . Note that the integrated intensity of B2 at both resonance energies and D1 at the $E_{t_{2g}}$ resonance are fixed in the whole temperature range as explained in Sec. S3D.

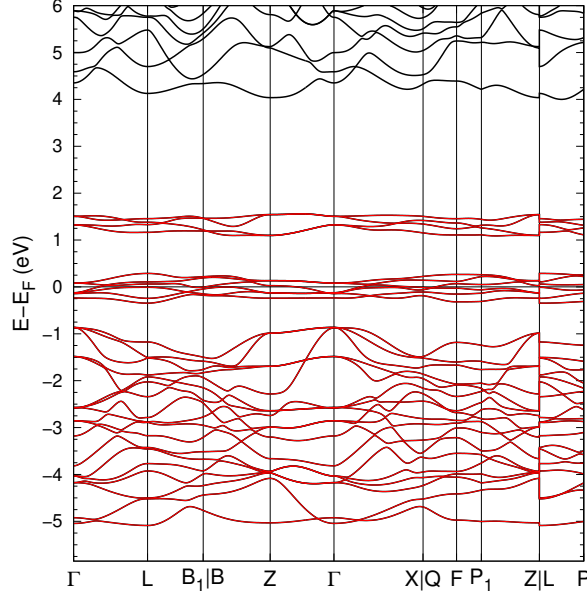


FIG. S14. Band structure of CrI_3 without spin-orbit coupling. Wannier projected bands are in red, overlain on the DFT calculated bands in black showing their agreement.

TABLE S1. **Full list of parameters used in the single site atomic model calculations.** $F_{dd,i}$ and $F_{dd,n}$ are for the initial and intermediate states, respectively. Units are eV.

$10D_q$	$F_{dd,i}^2$	$F_{dd,i}^4$	$F_{dd,n}^2$	$F_{dd,n}^4$	F_{dp}^2	G_{dp}^1	G_{dp}^3	ζ_i	ζ_n	ζ_c
1.50	6.574	4.121	7.074	4.435	3.067	2.250	1.279	0.035	0.047	5.667

S5. FURTHER DETAILS OF ED RIXS CALCULATIONS

To verify the suitability of the hopping matrix in the main text, we overlay the Wannier projected bands with the original density functional theory (DFT) in Fig. S14. We also provide further details of our atomic model for CrI_3 and the spin and angular dependence of the spectra.

A. Single site atomic model

We also tested a simpler model that only considers a single Cr^{3+} ion with 10 effective $3d$ orbitals. In this case, only three independent parameters are used, including k_{dd} , k_{dp} and $10D_q$. Again, k_{dd} dictates the energies of the dark excitons D1 and D2, and k_{dp} affects the resonance profiles of the excitations. Therefore, their refined values ($k_{dd} = 0.61$, $k_{dp} = 0.47$) are very close to that in the Anderson impurity model (AIM). However, the energy of exciton B1 is exclusively governed by $10D_q$, which gives $10D_q = 1.5$ eV. However, this choice of $10D_q$ limits the energy of exciton B2 to ~ 2.3 eV, much higher than the experimental value of 1.88 eV. Therefore, without explicitly including the ligand orbitals, we could not simultaneously obtain the correct energies for both B1 and B2. A comparison between the two models is displayed in Fig. S15, with the full parameters presented in Tab. S1. The failure of the atomic model further underlines the fact that CrI_3 is a self-doped charge transfer material.

B. XAS state analysis

We use $E_{t_{2g}}$ and E_{e_g} to label the resonance energies at $E_i = 575.1$ eV and 576.3 eV. To support this assignment, we calculated the relevant quantum numbers for the intermediate state in the atomic model approximation, which captures the resonance behavior reasonably well as shown in Fig. S15. The result is presented in Fig. S16. As expected, there is strong mixing between t_{2g} and e_g orbitals, however, a substantial change in t_{2g} vs. e_g is seen, confirming that

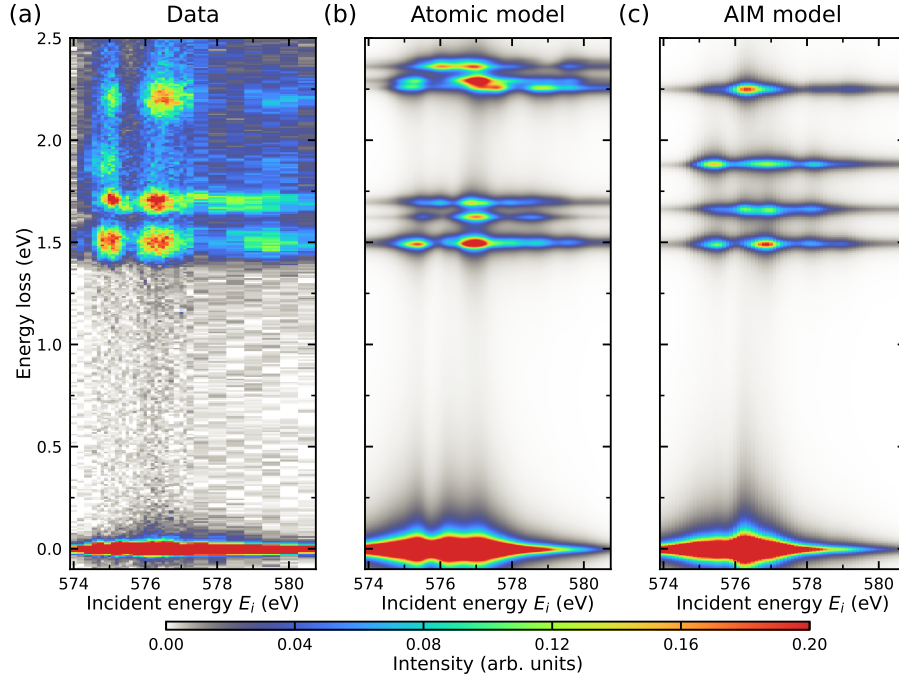


FIG. S15. Comparison of RIXS energy maps calculated using different models. (a) The measured RIXS energy map. (b) The calculated RIXS energy map using an atomic model. (c) The calculated RIXS energy map using an AIM. Panels (a),(c) use the same data shown in Fig. 4(a)–(b) and are replotted here for comparison.

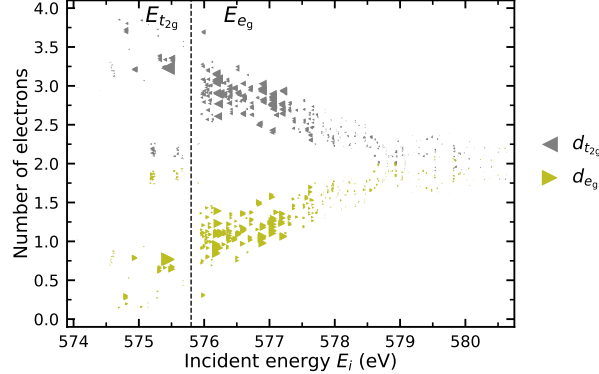


FIG. S16. Electron occupations of t_{2g} and e_g orbitals in the intermediate state of the atomic model. The symbol size (area) is proportional to the calculated intensity of each state.

our labels are reasonable.

C. Angular dependence

In the measured in-plane momentum dependence of the RIXS spectra, we observe that the intensity of the D1 exciton reaches its maximum near the Brillouin zone center at $E_{t_{2g}}$ resonance. This trend is qualitatively captured by the angular dependence of the calculated RIXS spectra. In Fig. S17, we show the calculated intensity of this exciton D1 as a function of the incident angle θ at $E_{t_{2g}}$ resonance using the AIM. By varying the incident angle, we essentially change the polarization of the incident and scattered photons, which ultimately affects the RIXS cross section.

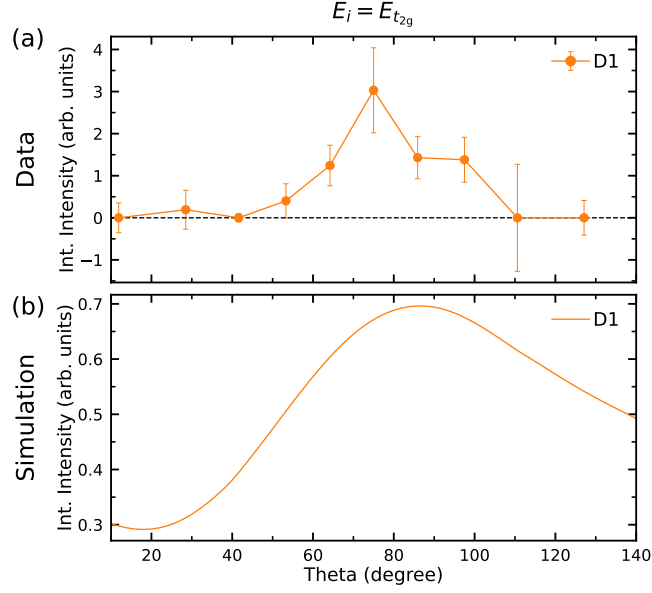


FIG. S17. Comparison between the measured and calculated incident-angle theta dependent dark exciton D1 intensity at $E_{t_{2g}}$ resonance. The calculation is based on the AIM. The calculation nicely reproduces the trend of the intensity.

D. Spin direction dependence

We have shown an abrupt change in the dark exciton intensity across the FM transition temperature T_c . Here, we examine one possible origin by considering the spin-direction dependent RIXS spectra. The rationale is that the spin direction, which is clearly different across T_c , can potentially affect the RIXS cross section. Below T_c , CrI_3 is in the FM state with spins pointing along c -axis, whereas above T_c , it enters the paramagnetic state with randomly oriented spins. This change in spin direction can be simulated by controlling the direction of the external magnetic field \mathbf{B} in the Zeeman term. The representative calculated spectra based on the AIM are shown in Fig. S18. The calculated dark exciton intensity barely changes in comparison to the bright excitons, contrary to the trends observed from the experimental spectra. Thus, the peculiar temperature dependence cannot be simply explained by the spin-direction dependence and likely requires more complicated explanations involving exciton-magnon interactions.

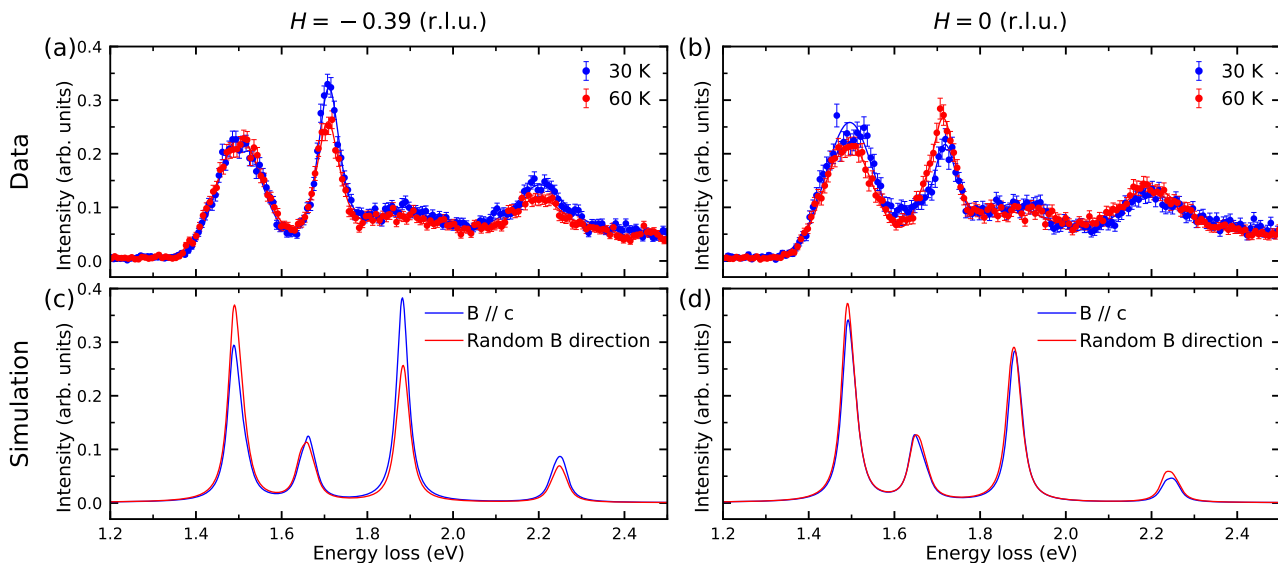


FIG. S18. Comparison between the measured and calculated RIXS spectra. (a),(b) Representative measured RIXS spectra at two different momentum transfers at two temperatures. The solid lines are the fits to the data. Blue data is within the magnetically ordered phase well below the FM transition temperature T_c , whereas red data is near T_c with much reduced ordered moment. (c),(d) Corresponding calculated RIXS spectra based on the AIM to simulate the spin direction effect. The blue lines assume the spin directions are aligned along the c -axis, while the red lines assume random spin directions. The calculations predict negligible changes in the intensities of the dark excitons, in contrast to the experimental observations.

S6. AN ASIDE ON TERMINOLOGY

Here, we further discuss whether the excitations in CrI_3 should be classified as dd -excitations or, more generally, as excitons. This requires a precise definition of dd -excitations. The strictest definition involves transitions that, to a good approximation, occur only within local d -orbitals. A broader but still rigorous definition describes dd -excitations as transitions within an effective manifold of hybridized d -orbitals centered on the transition metal site in an atomic-like model. Based on either definition, it is clear that CrI_3 does not host strictly defined dd -excitations (see Fig. 4 of the main text and Sec. S5 A).

However, less stringent definitions of dd -excitations are sometimes employed in the literature. The term dd -excitation is generally less likely to be used for a transition that exhibits interesting coupling to magnetism, but there are exceptions here. The terms exciton and dd -excitation are also sometimes associated with narrow and broad linewidths, respectively, but to our knowledge, no attempt has been made to quantify the boundary between these categories. Furthermore, as linewidths depend on material purity and temperature, such distinctions are not necessarily meaningful. The overwhelming majority of papers consider dd -excitation local transitions not dispersive quasiparticles.

Our newly discovered 1.7 eV transitions in CrI_3 are dispersive, exhibit temperature dependence across the magnetic transition, and display narrow linewidths both in general and compared to other transitions in the material. All these properties are more compatible with the use of the term exciton than the typical use of the term dd -excitation. Despite the partial ambiguity, we conclude that D1 and D2 are best termed excitons.

